The Astrophysical Journal, 929:60 (23pp), 2022 April 10 https://doi.org/10.3847/1538-4357/ac5632

Dissecting the Different Components of the Modest Accretion Bursts of the Very Young Protostar HOPS 373

Sung-Yong Yoon[1,2], Gregory J. Herczeg[3,4], Jeong-Eun Lee[1], Ho-Gyu Lee[2], Doug Johnstone[5,6], Watson Varricatt[7], John J. Tobin[8], Carlos Contreras Peña[9,10], Steve Mairs[11], Klaus Hodapp[12], P. Manoj[13], Mayra Osorio[14], and S. Thomas Megeath[15]
the JCMT Transient Team

[1] The School of Space Research, Kyung Hee University, 1732 Deogyeong-daero, Giheung-gu, Yongin-si, Gyeonggi-do, Republic Of Korea; gherczeg1@gmail.com, jeongeun.lee@khu.ac.kr
[2] Korea Astronomy and Space Science Institute, 776, Daedeok-daero, Yuseong-gu, Daejeon, 34055, Republic Of Korea
[3] Kavli Institute for Astronomy and Astrophysics, Peking University, Yiheyuan 5, Haidian Qu, 100871 Beijing, People's Republic of China
[4] Department of Astronomy, Peking University, Yiheyuan 5, Haidian Qu, 100871 Beijing, People's Republic of China
[5] NRC Herzberg Astronomy and Astrophysics, 5071 West Saanich Road, Victoria, BC, V9E 2E7, Canada
[6] Department of Physics and Astronomy, University of Victoria, 3800 Finnerty Road, Elliot Building, Victoria, BC, V8P 5C2, Canada
[7] UKIRT Observatory, University of Hawaii, Institute for Astronomy, 640 N. Aohoku Place, Hilo, HI 96720, USA
[8] National Radio Astronomy Observatory, 520 Edgemont Road, Charlottesville, VA 22903, USA
[9] Physics and Astronomy, University of Exeter, Stocker Road, Exeter EX4 4QL, UK
[10] Centre for Astrophysics Research, University of Hertfordshire, Hatfield AL10 9AB, UK
[11] East Asian Observatory, 660 N. A'ohoku Place, Hilo, HI 96720, USA
[12] University of Hawaii, Institute for Astronomy, 640 N. Aohoku Place, Hilo, HI 96720, USA
[13] Tata Institute of Fundamental Research, Homi Bhabha Road, Mumbai 400 005, India
[14] Instituto de Astrofisica de Andalucia, CSIC, Glorieta de la Astronomia S/N, E-18008, Grenada, Spain
[15] Ritter Astrophysical Research Center, Department of Physics and Astronomy, University of Toledo, W. Bancroft Street, Toledo, OH 43606 USA
Received 2021 September 5; revised 2022 February 7; accepted 2022 February 10; published 2022 April 13

Abstract

Observed changes in protostellar brightness can be complicated to interpret. In our James Clerk Maxwell Telescope (JCMT) Transient Monitoring Survey, we discovered that a young binary protostar, HOPS 373, is undergoing a modest 30% brightness increase at 850 μm, caused by a factor of 1.8–3.3 enhancement in the accretion rate. The initial burst occurred over a few months, with a sharp rise and then a shallower decay. A second rise occurred soon after the decay, and the source is still bright one year later. The mid-IR emission, the small-scale CO outflow mapped with ALMA, and the location of variable maser emission indicate that the variability is associated with the SW component. The near-IR and NEOWISE W1 and W2 emission is located along the blueshifted CO outflow, spatially offset by ~3 to 4″ from the SW component. The *K*-band emission imaged by UKIRT shows a compact H_2 emission source at the edge of the outflow, with a tail tracing the outflow back to the source. The W1 emission, likely dominated by scattered light, brightens by 0.7 mag, consistent with expectations based on the submillimeter light curve. The signal of continuum variability in *K* band and W2 is masked by stable H_2 emission, as seen in our Gemini/GNIRS spectrum, and perhaps by CO emission. These differences in emission sources complicate IR searches for variability of the youngest protostars.

Unified Astronomy Thesaurus concepts: Stellar jets (1607); Variable stars (1761); Stellar accretion disks (1579); Submillimeter astronomy (1647); Protostars (1302)

Supporting material: machine-readable tables

1. Introduction

Accretion outbursts are thought to play an important role in the growth of the protostar and in the evolution of its disk. Historically, most accretion bursts were discovered with optical variability and are therefore identified during the later stages of protostellar evolution, after the star has already grown to near its final mass and has shed its envelope (see reviews by Hartmann & Kenyon 1996 and Audard et al. 2014 and subsequent discoveries from Gaia by, e.g., Hillenbrand et al. 2018 and Szegedi-Elek et al. 2020). However, accretion outbursts may play an even more important role at the youngest stages of stellar growth, as indicated by indirect probes such as outflow knots (e.g., Reipurth 1989; Plunkett et al. 2015), envelope chemistry (e.g., Lee 2007; Jørgensen et al. 2015; Hsieh et al. 2019), and by models of disk instabilities (e.g., Bae et al. 2014). A few accretion outbursts have been detected toward very young low-mass protostars (e.g., Kóspál et al. 2007; Safron et al. 2015; Kóspál et al. 2020).

Over the past few years, several surveys at longer wavelengths have been designed to statistically evaluate accretion variability at earlier stages of protostellar evolution (e.g., Scholz et al. 2013; Antoniucci et al. 2014; Rebull et al. 2014; Lucas et al. 2017; Johnstone et al. 2018; Fischer et al. 2019; Lee et al. 2021; Park et al. 2021; Zakri et al. 2022), when the star is still in its main growth phase and the disk is accreting from the envelope. For protostars, submillimeter (submm) emission is produced by warm dust in the envelope (and disk), serving as a bolometer that can be converted into a luminosity (e.g., Johnstone et al. 2013; MacFarlane et al. 2019a, 2019b;

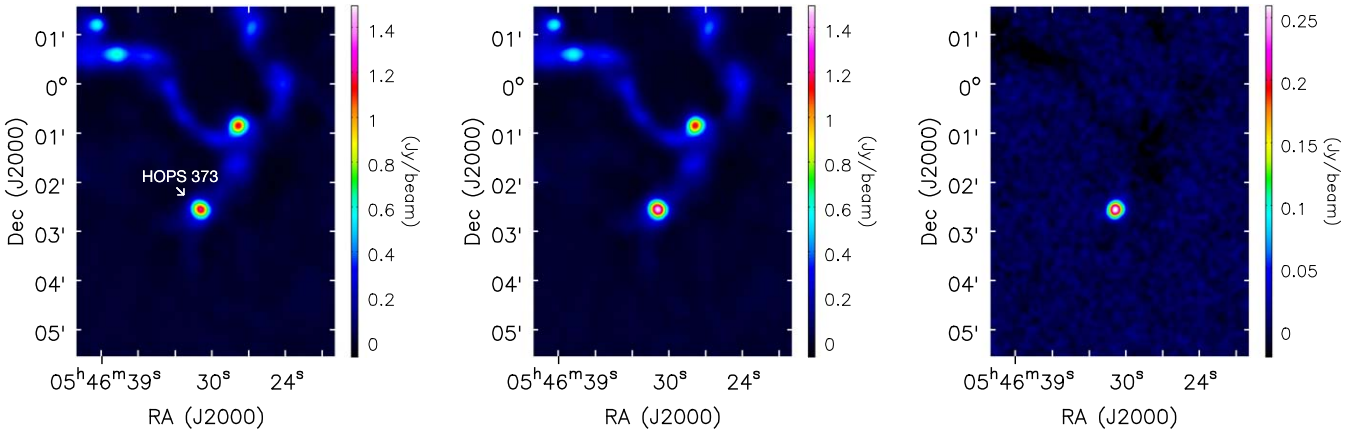

Figure 1. SCUBA-2 850 μm continuum images of HOPS 373 in the quiescent phase (left, coadded from 14 epochs in 2017), in the burst phase (center, coadded from 12 epochs in 2020–2021), and the residual (burst minus quiescent) image (right).

Baek et al. 2020). However, the IR emission from deeply embedded objects may be much more complicated because this emission may escape only through optically thin outflow cavities (e.g., Lee et al. 2010; Herczeg et al. 2012; Tobin et al. 2020a). In three previous cases, varying IR emission has been resolved into scattered-light nebulae surrounding embedded protostars (Muzerolle et al. 2013; Balog et al. 2014; Carattio et al. 2015; Cook et al. 2019).

In this paper, we dissect the ongoing, modest accretion outburst of HOPS 373 as seen in near-IR, mid-IR, submm, millimeter (mm), and centimeter (cm) observations. The central protostar has characteristics that are typical of a very young protostar driving a powerful outflow. The protostellar envelope of HOPS 373 was initially identified in submm mapping of NGC 2068 (distance of 428 pc; Kounkel et al. 2018) in the Orion B cloud complex (Johnstone et al. 2001; Phillips et al. 2001; Motte et al. 2001), following the discovery of a large CO outflow (Gibb & Little 2000) and a nearby maser (Haschick et al. 1983). From fits to the near-IR through mm spectral energy distribution, the protostar has a bolometric luminosity of 5.3–6.1 $L_{\odot}$ and a bolometric temperature of 37 K (Kang et al. 2015; Furlan et al. 2016). The spectral energy distribution (SED), with a total-to-submm luminosity ratio of 34, is red enough to be a PACS Bright Red Source (Stutz et al. 2013) and consistent with an early stage of a Class 0 protostar. HOPS 373 and its associated outflows are not detected in X-rays (Getman et al. 2017). The central object was resolved with high-resolution mm interferometry into two distinct mm peaks separated by $3\farcs6$, or 1500 au (Tobin et al. 2015, 2020b). The source drives a powerful outflow. Submillimeter CO emission from the large-scale outflow extends over 1 arcmin to both the blue (southeast) and red (northwest) directions with a dynamical time of 10^4 yr (Mitchell et al. 2001; Nagy et al. 2020). Far-IR spectra reveal excited molecular emission that likely traces the walls of an outflow cavity (Tobin et al. 2016), with far-IR CO emission that is the brightest of all PACS Bright Red Sources and among the brightest of all low-mass protostars (Manoj et al. 2016; Karska et al. 2018).

The NGC 2068 star-forming region, including HOPS 373, has been monitored in the submm by the James Clerk Maxwell Telescope (JCMT) Transient Survey since 2015 December (Herczeg et al. 2017). Beginning in 2016, HOPS 373 had gotten fainter by 10% (Johnstone et al. 2018) and stayed steady in this lower luminosity state until a brief increase of 25% in late 2019 (Lee et al. 2021), a pattern also seen at 4.5 μm with NEOWISE (Contreras Peña et al. 2020; Park et al. 2021). We report that HOPS 373 has since returned to the bright state in the submm, and analyze in detail the location of emission across the spectrum. We combine the submm light curve with near-IR spectroscopy and imaging to dissect how the source is seen across a range of diagnostics. In Section 2 we describe the array of observations that is used in this paper. In Section 3 we describe the submm and NEOWISE light curves and provide a physical interpretation for the submm variability. In Section 4 we describe the morphology of the emission sources. In Section 5 we present Gemini/GNIRS spectra to demonstrate the dominance of H_2 emission in the *K*-band imaging. In Section 6 we interpret these results and discuss their importance in ongoing and future searches for variable protostars.

2. Observations

2.1. Submillimeter Monitoring at 450 and 850 μm

The JCMT Transient Survey (Herczeg et al. 2017) has been using SCUBA-2 (Holland et al. 2013) on the JCMT to monitor emission at 450 and 850 μm from eight regions every month, including NGC 2068, beginning in 2015 December. We also include an earlier data point from the JCMT-Gould Belt Survey (Kirk et al. 2016) obtained from 2014 November 16–22, reported and reanalyzed by Mairs et al. (2017a). In 2019 November, we discovered that HOPS 373 had brightened, and we increased our observational cadence of NGC 2068 to once every two weeks (Figure 1).

JCMT Transient Survey observations occur only when the precipitable water vapor content is $<$2.58 mm (opacity of $<$0.12 at 225 GHZ), corresponding to JCMT weather bands 1–3. Because of telluric absorption, the 450 μm imaging is only useable from the $\sim$50% of our observations that occur during epochs with the lowest precipitable water vapor content.

A full description of the data, advanced reduction, relative alignment, and calibration process developed by the JCMT Transient Survey is provided by Mairs et al. (2017b) for the 850 μm data and by S. Mairs et al. (2022, in preparation) for the 450 μm data. For HOPS 373, a bright submm source, the relative flux calibration is typically accurate to 2% at 850 μm

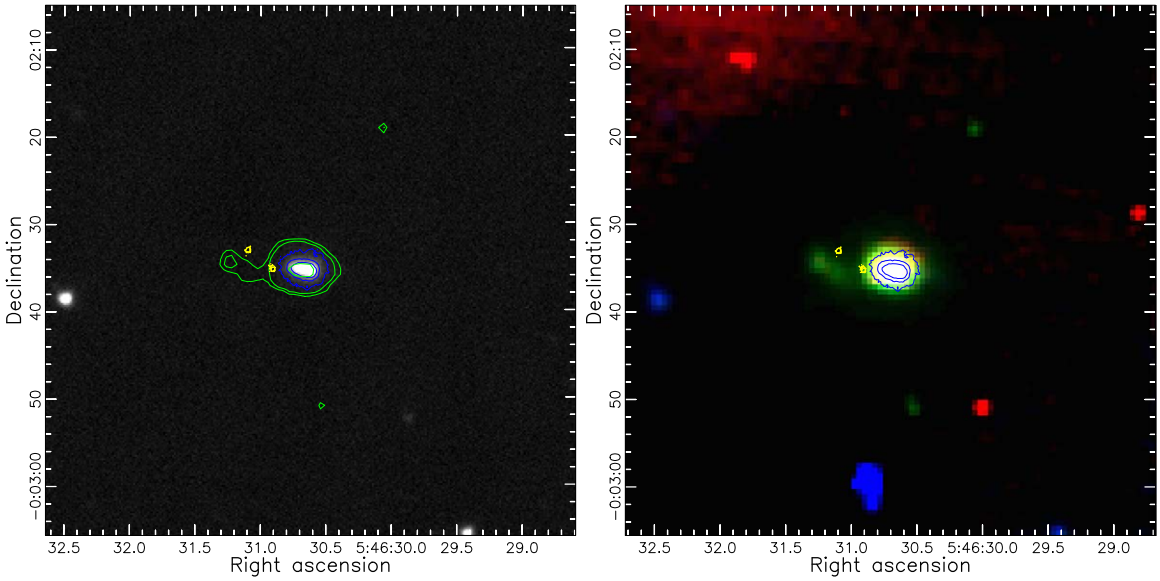

Figure 2. A $1' \times 1'$ field around HOPS 373 from (left) UKIRT *K*-band imaging and from (right) Spitzer/IRAC imaging in Band 1 (3.6 μm; blue), Band 2 (4.5 μm; green), and Band 4 (8 μm; red). Both images also show blue contours (99.9, 99.8, and 99.5 percentiles) from UKIRT 2.122 μm H_2 imaging and the yellow contours (99.5 and 99.0) from emission in the ALMA 890 μm continuum map; the left image shows green contours (99.9, 99, and 98.5) from Spitzer IRAC 4.5 μm imaging.

and ∼5% at 450 μm. The effective beam sizes are $14\farcs1$ and $9\farcs6$ at 850 and 450 μm, respectively (Dempsey et al. 2013; Mairs et al. 2021).

The absolute alignment of the SCUBA-2 images is uncertain by $\sim 2''$. Six objects in the field are compact, bright enough for centroid, and have a well-identified WISE or 2MASS counterpart. The position of HOPS 373 is shifted to the average WISE position of these objects, with a standard deviation in the positional differences of $1\farcs4$. However, possible systematics across the field[16] limit our confidence to $2''$.

2.2. Mid-Infrared Imaging from 3–24 μm

The Wide-field Infrared Survey Explorer (WISE; Wright et al. 2010) surveyed the entire sky in four bands, W1 (3.4 μm), W2 (4.6 μm), W3 (12 μm), and W4 (22 μm) with angular resolutions of $6\farcs1$, $6\farcs4$, $6\farcs5$, and $12''$, respectively, from January to 2010 September. After the depletion of hydrogen from the cryostat, the NEOWISE Post-Cryogenic Mission (Mainzer et al. 2011, 2014) has been observing the full sky in W1 and W2 at a six-month cadence since late 2013. HOPS 373 has been observed in March and September each year from 2014–2020.

Each epoch consists of ∼10–20 exposures taken over a few days. Each set of exposures is averaged to produce a single photometric point per epoch (following Contreras Peña et al. 2020). No significant variability is identified within each epoch.

We identify consistent seasonal offsets in the NEOWISE position of HOPS 373, as observed during fainter epochs. In March, the average position in W1 is located $0\farcs109 \pm 0\farcs018$ west and $0\farcs152 \pm 0\farcs016$ south of the average position in September; for W2, the September position is $0\farcs120 \pm 0\farcs016$ west and $0\farcs149 \pm 0\farcs016$ south. The average standard deviation in the seasonal position in a filter is $0\farcs024$ in each direction, which we adopt for the uncertainty in individual measurements. We are not aware of the reason for these seasonal differences and do not know whether they are common.

The field of HOPS 373 was observed multiple times using the Spitzer Space Telescope and the Infrared Array Camera (Fazio et al. 2004) in IRAC bands 1, 2, 3, and 4, centered at 3.6, 4.5, 5.8, and 8 μm, respectively. We obtained and averaged IRAC images from three AORs (4105472, 4105728, and 4105984) from the Spitzer Heritage Archive. Figure 2, right, shows a color-composite image in a $1' \times 1'$ field extracted from the averaged images in Band 1 (blue), Band 2 (green), and Band 4 (red). The near-IR counterpart of HOPS 373 has excess IRAC Band 2 emission, consistent with classification as an extended green object (EGO; Cyganowski et al. 2008).

The Spitzer/MIPS scan map observing mode covered the NGC 2068 region on 2004 March 15. We obtained the MIPS images at 24 μm, with the AOR of 4320256 from the Spitzer Heritage Archive.

2.3. Far-Infrared Imaging from 70–160 μm

The Herschel Space Observatory (Pilbratt et al. 2010) surveyed protostars in Orion star-forming regions (Stutz et al. 2013) with PACS 70 and 160 μm photometry. The PACS 70 and 160 μm data of HOPS 373 were acquired over an $8' \times 8'$ field size with beam sizes of $5\farcs6$ and $10\farcs7$, respectively. We obtained the PACS images of HOPS 373 observed on 2010 September 28 and 2011 March 6 from the Herschel science archive with the observation IDs of 1342205216, 1342205217, 1342215363, and 13422115364 (Fischer et al. 2020).

2.4. Monitoring at 2.2 μm and Imaging from 1–2.5 μm

We monitored HOPS 373 at near-IR wavelengths using the Wide Field Camera (WFCAM; Casali et al. 2007) on the 3.8 m UKIRT telescope from 2012 February to 2021 March. WFCAM employs four 2048×2048 HgCdTe Hawaii II arrays at an image scale of $0\farcs4$ pixel^{-1}. The object was dithered to nine positions separated by a few arcsecs, with 2×2 microsteps at each dither position to achieve an image scale of

[16] Matching 2MASS and WISE coordinates with compact SCUBA-2 sources in the Ophiuchus star-forming region yields $\sim 2''$–$3''$ trends across the image. This trend is unexplained.

$0\farcs2\,\mathrm{pixel}^{-1}$ in the final mosaics. The observations were obtained using the *J*, *H*, and *K* MKO filters centered at 1.25, 1.65, and 2.2 μm, respectively, and in a narrow-band filter centered at the wavelength of the H_2 1–0 S(1) line at 2.1218 μm. The monitoring comprised a set of shallow observations (1 s × 2 coadds per frame; 72 s integration per mosaic) in *J*, *H*, and *K* filters from 2012 to 2021 and observations with deeper integration in *K* (2 s × 5 coadds per frame; 360 s integration per mosaic) from 2020 September to 2021 March. The magnitudes are derived using the average zeropoints estimated from a set of isolated point sources, with absolute scaling from images obtained on a clear, photometric night. Data points are discarded if the the standard deviation of the zeropoints on the derived field stars is larger than 0.03 mag.

We observed HOPS 373 in the H2 line in eight epochs. The dither and microstep patterns were similar to those in K, but with a per frame exposure time of 40 s. This gives a total integration time of 1440 s for the mosaic from each epoch. The H_2 images are continuum-subtracted using the *K*-band images obtained closest in time and with the best agreement in seeing. The background-subtracted *K*-band image is divided by the average ratio of counts $[K/H_2]$ obtained for a few isolated point sources in the *K* and H_2 images. This image is then subtracted from the background-subtracted H_2 image to obtain the continuum-subtracted emission line image. Since clouds were present during some of these observations, the continuum-subtracted images from the different epochs were weighted according to the extinction from clouds and averaged.

The near-IR emission from HOPS 373 consists of a compact source with a tail. The magnitudes for these components, presented in Table 1, are estimated in two apertures of diameter 2″, centered on the compact source at $\alpha = 5{:}46{:}30.631$ $\delta = -00{:}02{:}35.43$ (J2000) and on the tail closer to the young stellar object (YSO), 1.″74 NE of the first position. Figure 2 shows a 1′×1′ field surrounding HOPS 373 in *K*, generated from the average of the *K*-band images from the epochs with deeper integration. The contours derived from the averaged continuum-subtracted H_2 image are overlaid on the *K*-band image.

We also obtained an acquisition image with Gemini North/GNIRS for our spectrum (Section 2.5). Because HOPS 373 shows extended structure in the near-IR, seven *K*-band acquisition images were taken to locate the GNIRS slit position precisely. Each image consists of 12 coadded frames with an exposure time of 2 s. A blank-sky image was generated by combining seven images after masking the emission region; it was then used for background subtraction and flat-fielding. The total exposure time of the integrated image is 168 s. The pixel size of 0.″15 and position angle of 157.°49 were used to place the imaging scale and orientation on the sky.

Table 1
Selected *K*-band Photometry[a]

MJD	Brt (mag)	Err (mag)	Tail (mag)	Err (mag)	t_{exp} (s)
51,093.310	15.22 ± 0.16		summed 2MASS K_S[b]		
55,164.335	15.037 ± 0.029		summed VISTA K_S[c]		
55,984.308	15.74	0.02	16.26	0.03	72
56,262.376	15.67	0.03	16.09	0.04	72
57,990.635	15.67	0.02	16.32	0.03	72
58,566.254	15.70	0.03	16.28	0.05	72
58,812.650	15.67	0.02	16.25	0.03	72
58,814.551	15.67	0.02	16.25	0.03	72
58,818.513	15.71	0.03	16.28	0.04	72
59,075.633	15.63	0.02	16.03	0.03	72
59,103.641	15.61	0.02	16.11	0.02	72
59,105.629	15.59	0.02	16.14	0.03	72
59,100.576	15.62	0.02	16.15	0.02	360
59,105.588	15.62	0.02	16.16	0.02	360
59,114.569	15.61	0.02	16.11	0.02	360
59,118.632	15.59	0.02	16.11	0.02	360
59,122.538	15.59	0.02	16.14	0.02	360
59,132.591	15.60	0.02	16.10	0.02	360
59,136.594	15.57	0.02	16.07	0.02	360
59,144.565	15.57	0.02	16.10	0.02	360
59,161.540	15.59	0.02	16.07	0.02	360
59,172.479	15.57	0.02	16.05	0.02	360
59,229.241	15.55	0.03	16.05	0.03	360
59,247.368	15.57	0.03	15.97	0.03	360
59,257.290	15.62	0.02	16.08	0.02	360
59,277.303	15.55	0.02	15.96	0.02	360
59,295.228	15.49	0.02	15.85	0.02	360
59,436.638	15.48	0.02	15.86	0.03	72
59,451.640	15.51	0.02	15.87	0.02	72
59,477.540	15.51	0.02	15.92	0.03	72

Notes.
[a] Full table available online, selected points shown here.
[b] Includes bright compact object and tail.
[c] Extended source extraction with 5.″7 diameter aperture. From McMahon et al. (2013).

(This table is available in its entirety in machine-readable form.)

2.5. Spectroscopy from 1.9–2.5 μm

We obtained a near-IR *JHK* spectrum of HOPS 373 using GNIRS on Gemini North in fast-turnaround time, program GN-2020B-FT-110 (PI: Doug Johnstone) on 2020 October 3 (HJD = 2,459,126.12). The integration time was 2400 s, split into two ABBA sequences with individual exposures of 300 s.

The data were obtained in the cross-dispersed mode with the 32 mm grating, the short camera, and a 0.″3 slit to achieve $R = 1700$ spectra from 1–2.5 μm. Our focus here is on the *K*-band spectrum because little emission is detected in *H* and none in *J*. The slit of 0.″3 × 7″ was aligned with the parallactic angle of 157.°49, almost perpendicular to the direction of the source extension, and centered on the compact source, which dominates the observed emission. The spectra were obtained at an average airmass 1.07. The data were reduced and extracted following standard techniques.

The data were corrected for telluric absorption using B8 V star HD 39803 observed immediately after HOPS 373 at an airmass of 1.14. The flux calibration of the HOPS 373 spectrum, with an estimated synthetic magnitude of $K = 15.56$, is estimated by the relative brightness to the same telluric standard star, as measured in the acquisition images, and assuming that the standard star is constant in brightness across the band.

The wavelength solution is accurate to ∼0.5 Å, or 7 km s^{-1}. However, each pixel covers 80–100 km s^{-1}, so any asymmetry in spatial extent of the source within the slit may cause additional shifts. We corrected for the local standard of rest (LSR) velocity frame using the IRAF task *rvcorrect*.

2.6. Radio Observations with the VLA

Observations toward HOPS 373 were conducted with the NSF's Karl G. Jansky Very Large Array (VLA) located on the

Plains of San Agustin in central New Mexico, USA. HOPS 373 was observed in multiple bands both before and after the outburst.

2.6.1. C-band Observations at 5 cm

Observations of HOPS 373 were conducted in *C* band at a central frequency of 6 GHz on 2015 October 6 (two executions) and on 2015 October 7, as part of archival program 15A-369. Both observations were obtained while the array configuration was transitioning from A to D configuration, with 21 useable antennas in D configuration. The 2015 October 7 data were unusable due to a system issue that occurred during observations. We performed subsequent observations on 2021 March 24 (program 21A–409) and 2021 May 15 (program 21A–423) in D configuration, replicating the setup of the archival observations. In 2015, J0541–0541 was used as the phase calibrator and 3C147 was used as the bandpass and flux calibrator. For 2021, we used J0552+0313 as the complex gain calibrator and 3C147 as the flux and bandpass calibrator.

We reduced and imaged the data using the VLA calibration pipeline in Common Astronomy Software Application (CASA; McMullin et al. 2007) version 6.1.2. The correlator was configured for 3 bit mode where the entire 4–8 GHz band is covered with a single setting. We performed additional flagging for system issues (amplitude jumps and spws total swamped with radio frequency interference, RFI) and reran the calibration pipeline. We imaged each observation using the CASA task *tclean* using *robust* = *0.5* weighting. We also cut out the inner 1.4 kλ baselines using the *uvrange* parameter to remove contributions from large-scale emission associated with the nearby H II region. The 2015 data were self-calibrated to remove dynamic range artifacts associated with a bright source in the field of view. The same source was substantially fainter during the 2021 observations, and therefore, self-calibration was not required.

For the 2021 observations, we restored the image using the same beam as the archival observations ($14\farcs77 \times 11\farcs40$) to perform data analysis with beam-matched data sets. The noise in each observation is 6.28, 5.35, and 4.88 μJy beam^{-1} in respective chronological order.

2.6.2. K-band Observations at 1.3 cm

D-configuration observations were conducted in *K* band (22 GHz) on 2015 October 17 and 2015 November 21 as part of program 15B–229. On 2021 April 5, we acquired additional D-configuration observations (program 21A–409). The 2015 observations used 8 bit samplers and observed spectral lines and continuum within two 1 GHz basebands. The main lines targeted were NH_3 (1,1), (2,2), (3,3), and the H_2O (water) maser transition ($J = 6_{1,6} \rightarrow 5_{2,3}$)) at 22.23507980 GHz. For the follow-up observations in 2021, we used 3 bit samplers to obtain the maximum continuum bandwidth, but also observed the same lines as observed in 2015. We only discuss the water maser emission and continuum data in this paper.

The data were all calibrated using the same methodology as described for *C* band. Imaging was performed with the CASA task *tclean* using *robust* = *0.5* for the continuum data and *robust* = *2* for the line data with 0.5 km s^{-1} channels. The noise in the continuum images is 7.2 and 10.7 μJy beam^{-1} for the 2015 and 2021 data, respectively, while the noise in the water maser data cubes is 1.23 and 5.55 μJy beam^{-1} for the 2015 and 2021 data, respectively.

2.6.3. Ka-band Observations at 9 mm

Observations were conducted in C configuration at Ka band (33 GHz) on 2016 January 30 as part of program 16A–197 and again on 2021 April 7 in D configuration (program 21A–409). Both observations used the 3 bit samplers to cover a total bandwidth of 8 GHz, but in 2021, we centered the two 4 GHz basebands at ~29 and 37 GHz to sample a wider fractional bandwidth.

The data were all calibrated using the same methodology as described for *C* band. Imaging was performed with the CASA task *tclean* using *robust* = *0.5* for the D-configuration data observed in 2021. Then for the C-configuration data, we used *robust* = *2.0* and *uvtaper* = *70 k*λ to better match the D-configuration beam.

2.6.4. Flux Density Measurements with the VLA

To measure the flux densities of the continuum sources in C, K, and Ka bands, we used the CASA imfit task to fit the source with two Gaussian profiles in K and Ka bands, where the sources are resolved, and a single Gaussian profile in *C* band, where the two sources are unresolved. We provided imfit with initial estimates for the position, flux density, and source size and allowed the fitting to converge on its own. At *C* band, we fixed the source size to be a point source.

For the *C*-band data, we also measured the flux densities of all sources that appeared in both the 2015 and 2021 data beccause numerous YSOs and background sources lie within the field of view. This enables us to characterize any systematic offsets in flux density calibration. Twenty-five sources detected in both the 2015 and 2021 observations show a median variation of +15 μJy, with a corresponding median flux density ratio of 1.22. Similarly, for the two 2021 epochs, 28 matched sources show a median variation of +1 μJy, with a corresponding median flux density ratio of 1.01.

The median flux density ratio of 1.22 for the 2015 to 2021 epoch is higher than the expected flux density uncertainty of 5%–10% in *C* band. Furthermore, the same absolute flux calibrator (3C147) was used for both the 2015 and 2021 observations, and the calibrator has had consistent flux density within ~1% between 2016 and 2019. We therefore expect that the large difference of measured flux densities between epochs is due to real variability in the sources and not a flux density calibration error.

2.7. ALMA Observations

The Atacama Large Millimeter/submillimeter Array (ALMA), located in northern Chile on the Chajnantor plateau at an elevation of ~5000 m, consists of 50 12 m antennas that constitute the main 12 m array, ten 7 m antennas that form the ALMA Compact Array (also called the Morita Array), and an additional four 12 m antennas that are used for total power observations. The analysis of HOPS 373 makes use of data from standalone observations with the ACA and the 12 m array. No data combination is performed.

2.7.1. ACA Observations at 1.33 mm

The Atacama Compact Array (ACA) and Total Power (TP) antennas conducted the Band 6 observation toward HOPS 373 on 2019 March 21 as a part of program (2018.1.01565.S; PI: Tom Megeath). The beam size of the continuum is $4\farcs4 \times 6\farcs8$ and the reference frequency is 225.69 GHz (1.33 mm). The ^{12}CO $J = 2$–1 line (230.538 GHz) analyzed in this work is obtained from the spectral window with a reference frequency of 230.59 GHz and a bandwidth of 250.00 MHz. The spectral resolution is 0.317 km s^{-1}.

2.7.2. ALMA 12 m Array and ACA Observations at 0.89 mm

The observations of HOPS 373 with the 12 m array were conducted as part of program 2015.1.00041.S (PI: John J. Tobin) and were carried out in Band 7 on 2016 September 3 and 4, and on 2017 July 19. The time on HOPS 373 during each execution was ∼20 s for a total integration time of ∼1 minute. The maximum baseline length for the 2016 and 2017 observations was ∼2500 m and ∼3700 m, respectively. The correlator was configured to have two basebands observed in low-resolution continuum mode, each baseband having a bandwidth of 1.875 GHz divided into 128 channels that are 31.25 MHz wide. The other two basebands were configured for spectral line observations. The first was centered on ^{12}CO ($J = 3 \rightarrow 2$) at 345.79599 GHz, having a total bandwidth of 937.5 MHz and 0.489 km s^{-1} channels. The second spectral line baseband was centered on ^{13}CO ($J = 3 \rightarrow 2$) at 330.58797 GHz, having a total bandwidth of 234.375 MHz and 0.128 km s^{-1} channels. The line-free regions of the spectral line basebands were also used in the continuum imaging to result in an effective bandwidth of ∼4.75 GHz at 0.89 mm. Reduction of the raw data and subsequent imaging was performed using CASA version 4.7.2. Self-calibration was also performed on the continuum data to increase the signal-to-noise ratio (S/N), and the self-calibration solutions were also applied to the spectral line data. The resultant 0.89 mm continuum image created using the CASA task *clean* with *robust* = 0.5 has a beam of $\sim 0\farcs11$ and a noise of 0.27 mJy beam^{-1}. The ^{12}CO ($J = 3 \rightarrow 2$) image was created using natural weighting, but the visibilities were also tapered, starting at 500 kλ to increase sensitivity to large-scale structures, resulting in a $\sim 0\farcs25$ beam with a noise level of 20 mJy beam^{-1} (see Tobin et al. 2020b for further details about the observations and data analysis).

The ACA observation was conducted on 2018 October 2 as a part of program 2018.1.01284.S (PI: Tom Megeath). The continuum was observed with a beam size of $5\farcs0 \times 2\farcs9$ at a reference frequency of 338.239 GHz.

2.8. Gaia Astrometry of the Parent Association

HOPS 373 is likely associated with the NGC 2068-1 group described by Kounkel et al. (2018) from Gaia DR2 astrometry, located at 428 pc (Gaia Collaboration et al. 2018). The mean proper motion of this group is 0.254 mas yr^{-1} in R.A. and −0.573 mas yr^{-1} in decl.. This proper motion leads to spatial offsets of $\sim 0\farcs01$ between the 2MASS epoch and later epochs from ALMA and NEOWISE. This offset is negligible for our analysis and is not applied to our astrometry. The velocity relative to the local standard of rest ($v_{\rm lsr}$) is ∼10.3 km s^{-1} (e.g., Mitchell et al. 2001; Kang et al. 2015; Nagy et al. 2020).

3. Light curves of Spatially Unresolved Emission

In this section, we describe the time variability of HOPS 373 and present a fiducial model to explain the submm brightening as a response to increased accretion luminosity from a protostar deeply embedded in an envelope.

3.1. Qualitative and Quantitative Description of the Light Curves

The burst was initially detected in monitoring at 850 μm (Figure 1), triggering the follow-up investigation analyzed here. Figure 3 and Tables 1–3 present light curves for HOPS 373 in the submm, mid-IR, and near-IR. Figure 4 and Table 4 compare the size of the burst in each band.

Starting in 2015 December, HOPS 373 had an initial flux density of 1.3 Jy beam^{-1} at 850 μm for a few months, before decaying to a steady local minimum (quiescent) level of 1.2 Jy beam^{-1} by 2016 April. An early point from the Gould Belt Survey in 2014 November (Mairs et al. 2017a) is consistent with the initial level in 2015 December. HOPS 373 then brightened by 25% to 1.5 Jy beam^{-1} in 2019 September and decayed back to quiescence by 2020 March 7. By the next data point, in 2020 August, HOPS 373 was again bright and has stayed in this bright state in all epochs through the end of 2021. The SCUBA-2 450 μm data are noisier and sparser, but follow the same trend as the 850 μm measurements[17], with $F_{450} \propto F_{850}^{1.6\pm0.1}$.

The late 2019 outburst is narrower and more peaked in time than a Gaussian profile. The rise time is very uncertain and can be arbitrarily steep because only one point is clearly in the increasing part of the light curve. If the rise is exponential, the timescale near the peak must be shorter than 70 days (doubling time shorter than 50 days), based on the peak flux plus the one point in the rise. The decay is better constrained, with an e-folding timescale[18] of 105^{+35}_{-21} days (halving time of 73 days). The brightening of 30% from minima to maxima is the third largest change in flux seen in the JCMT Transient Survey to date, surpassed by only by HOPS 358 and Serpens Main EC 53 (Lee et al. 2021).

The NEOWISE mid-IR light curves also follow the same general pattern, with a lower cadence of one epoch every six months. The 2015–2016 decay occurred from a previous stable period that was 25% brighter in W1. HOPS 373 then stayed faint until February 2019, with a bright epoch in 2019 September, a faint epoch in 2020 March, and then another bright epoch in 2020 September. The NEOWISE epoch in late 2019 occurred about 8 days before the first SCUBA-2 peak, including one exposure just 4 days earlier. In 2020, the mid-IR returned to quiescence and then burst again, with an epoch 4 days after a SCUBA-2 observation. The two mid-IR bright measurements are 2.46 and 2.88 times brighter than quiescence at W1, but only 1.39 and 1.51 times brighter than quiescence at W2.

The *K*-band monitoring is consistent with the submm and mid-IR light curves, but with the scale of variability suppressed. Prior to the first burst, the *K*-band emission showed stochastic fluctuations within a 0.1 mag range that are consistent with a constant brightness. The *K*-band monitoring

[17] All uncertainties are 1σ.

[18] The decay is also consistent with a linear decay with a slope of $\sim(1.1 \pm 0.2) \times 10^{-3}$ Jy day^{-1}, although the peak itself would be an outlier inconsistent with this fit.

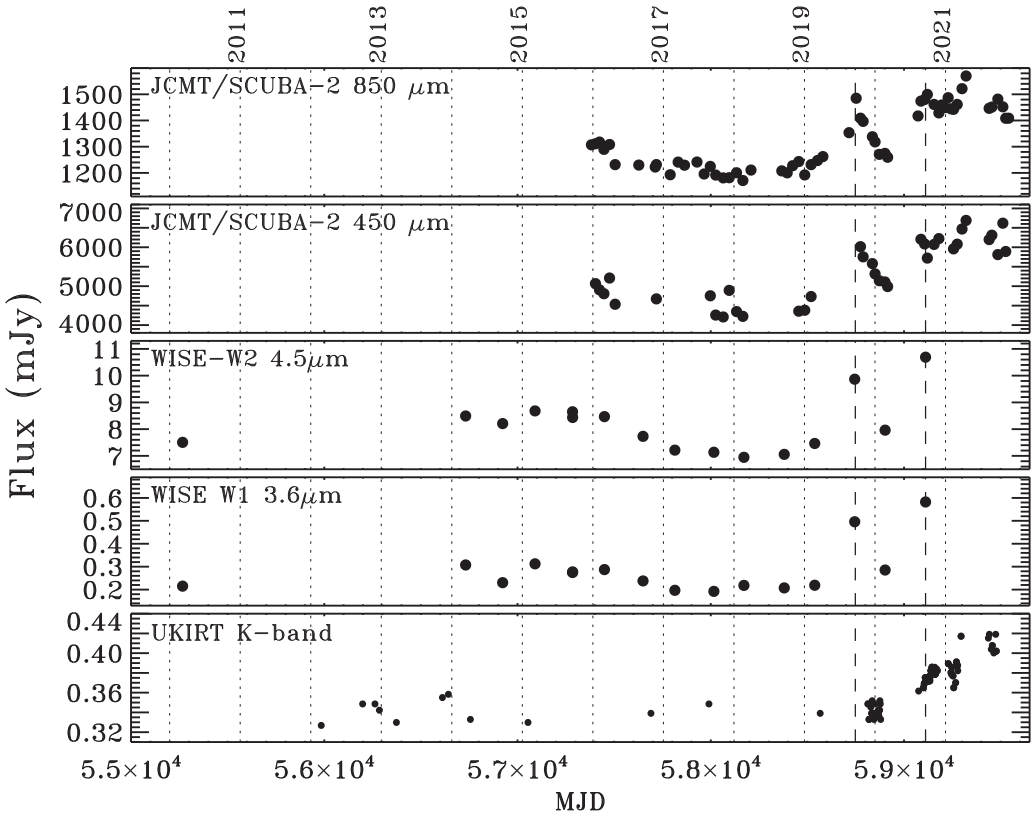

Figure 3. Light curves of HOPS 373 at 850 and 450 μm from JCMT/SCUBA-2, at 4.5 and 3.6 μm from WISE and NEOWISE, and in the *K* band with UKIRT. The dotted vertical lines mark January 1 for each year. The dashed vertical lines indicate the dates that are used for Table 4.

Table 2
Selected Submillimeter Peak Brightness[a]

MJD	450[b] (Jy beam^{-1})	850[b] (Jy beam^{-1})	MJD	450[b] (Jy beam^{-1})	850[b] (Jy beam^{-1})
57,403.348	5.07	1.31	58,850.285	5.32	1.32
57,424.223	4.91	1.32	58,872.391	5.14	1.27
57,505.215	4.54	1.23	58,915.297	4.99	1.26
57,997.668	4.75	1.22	59,072.633		1.42
58,025.621	4.26	1.19	59,087.645	6.21	1.47
58,095.422	4.89	1.18	59,106.723	6.09	1.48
58,133.410	4.35	1.20	59,155.480	6.07	1.46
58,486.270	4.38	1.19	59,180.371	6.22	1.43
58,519.336	4.73	1.23	59,256.199	5.96	1.44
58,580.258		1.26	59,275.273	6.08	1.46
58,715.621		1.35	59,300.223	6.47	1.52
58,752.539		1.48	59,321.219	6.69	1.57
58,774.727	6.02	1.41	59,454.633	6.31	1.45
58,788.465	5.75	1.40	59,485.562	5.81	1.48
58,836.355	5.58	1.34	59,541.398		1.41

Notes.
[a] Full table available online, selected points shown here.
[b] Error of 5% at 450 μm and 2% at 850 μm.

(This table is available in its entirety in machine-readable form.)

Table 3
Mid-IR Photometry from NEOWISE

MJD	W1 (mag)	Err (mag)	W2 (mag)	Err (mag)
55,266.88[a]	15.32	0.27	10.930	0.021
55,458.14[a]	15.49	0.38	10.933	0.026
56,731.57	15.01	0.24	10.765	0.031
56,923.07	15.32	0.50	10.802	0.040
57,090.68	14.99	0.24	10.741	0.029
57,284.77	15.13	0.42	10.745	0.036
57,285.24	15.12	0.25	10.772	0.024
57,449.77	15.08	0.26	10.768	0.038
57,649.51	15.29	0.30	10.867	0.037
57,814.28	15.49	0.40	10.942	0.036
58,016.13	15.52	0.42	10.954	0.040
58,171.58	15.38	0.36	10.983	0.035
58,380.29	15.44	0.35	10.966	0.032
58,537.98	15.38	0.33	10.905	0.031
58,744.87	14.49	0.15	10.602	0.033
58,902.25	15.09	0.24	10.835	0.035
59,111.60	14.31	0.14	10.515	0.036

Note.
[a] ALLWISE photometry from Cutri et al. (2021).

missed the first burst. The most recent points are ~0.15–0.25 mag brighter than those in quiescence.

The submm and mid-IR light curves follow each other closely, but with differences in the amplitude of change. Averaging the two bursts and comparing against the mean of the preceding quiescent period (Table 4), the minimum to peak increase is a factor of 2.66 (1.06 mag) at W1, 1.45 (0.40 mag) at W2, and 1.24 (0.23 mag) at 850 μm. Scaled to the 850 μm observations, both the W1 and W2 emission increased more during the 2020 peak than in the 2019 peak. However, this difference may be the consequence of the offset in time between the mid-IR and submm observations in the first burst. The higher cadence of submm observations and the long duration at a near-constant flux during the second burst makes the relative changes more reliable.

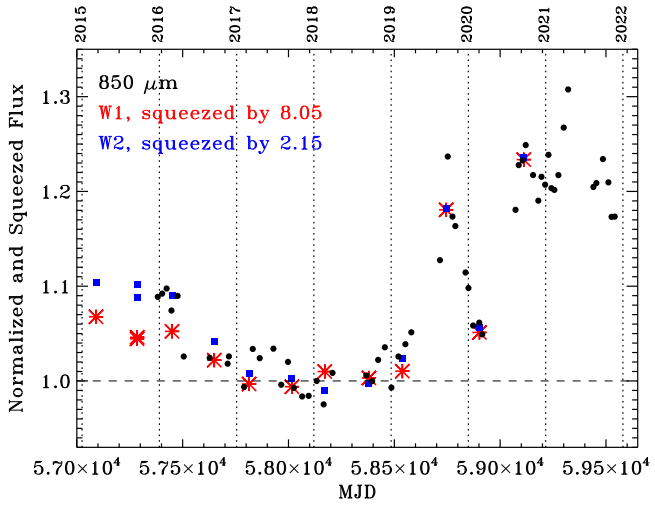

Figure 4. The submm and WISE light curves of HOPS 373. The WISE W1 (red asterisks) and W2 (blue squares) photometry is squeezed so that the change between the quiescent level and the most recent burst match the contemporaneous submm fluxes (black circles). The dotted vertical lines indicate January 1 for each year.

Table 4
Flux versus Wavelength[a]

MJD =	57,750–58,450	58748		59111[b]	
λ (μm)	Quiescent	Burst 1	Ratio	Burst 2	Ratio
2.2 comp[c]	3.42e-4	⋯	⋯	3.72e-4	1.087
2.2 tail[c]	1.97e-4	⋯	⋯	2.30e-4	1.170
3.6	2.02e-4	4.96e-4	2.46	5.82e-4	2.88
4.5	7.10e-3	9.87e-3	1.39	10.7e-3	1.51
450	4.30	⋯	⋯	5.91	1.37
850	1.20	1.485	1.24	1.490	1.24

Notes.
[a] All fluxes in Jy; ratios are burst/quiescent flux.
[b] Relative offsets from MJD = 59,111 may be more reliable; SCUBA-2 averaged from MJD 59,107 and 59,121.
[c] Compact source and tail in *K* band.

The previous *Spitzer* photometry is consistent with the WISE photometry,[19] with IRAC Band 1 of 13.86 and IRAC Band 2 of 10.79 mag (Stutz et al. 2013; Getman et al. 2017).

3.2. A Fiducial Model for the Submillimeter Light Curve

The variability in the submm light curve is likely a response to a luminosity change within the deeply embedded protostar. The variable emission at 850 μm, where the envelope is optically thin, is the consequence of a change in the dust temperature within the dense enshrouding envelope (see, e.g., Johnstone et al. 2013). Infrared wavelengths are closer to the peak of the SED and should directly trace the emission from the protostar and inner disk, but with interpretations that are complicated by uncertain optical depth effects, including scattering. As we show in Section 4, for this deeply embedded source, the outflow cavity is the surface of the last emission for the energy that escapes in the mid-IR, although that energy should trace changes in the emission from the central protostar and its disk.

For sufficiently low dust temperatures, the 450 μm emission is somewhat shortward of the Planck function Rayleigh–Jeans limit, such that small temperature changes result in a larger than linear brightness response. In contrast, the longer wavelength 850 μm emission is always closer to the Rayleigh–Jeans limit. Indeed, for a mean dust temperature in the envelope of 10—15 K at quiescence, the observed relation between the submm brightnesses, $F_{450} \propto F_{850}^{1.6}$, is well recovered, as the heating leads to a larger response at 450 μm versus 850 μm.

Along with the variation in the amplitude of brightness changes across wavelengths to underlying protostar luminosity changes, the Johnstone et al. (2013) model predicts a time delay for the submm emission due to the finite light propagation that is required for the dust heating within the envelope. The crossing time of a 5000 au core is about 30 days. Given that most of the core mass is on large scales, Johnstone et al. (2013) anticipated a smoothing of the light curve on timescales shorter than a month.

To roughly estimate the submm light curve, we model the time-dependent submm transport of energy through the envelope as a response to a jump in protostellar luminosity. Because the expected density and temperature profiles within the core decline as radial power laws outward from the center, the submm time response is not uniform, but rather highly peaked toward the first few days and with a long tail reaching out to months (heating the backside of the core introduces twice the delay from light travel time). Using this time-dependent response to fit the observed submm light curve in late 2019, we find that the limit on the exponential rise doubling time of the source shrinks to less than 30 days, while the ∼75-day decay halving time stays the same. The timing of the underlying burst, however, is shifted earlier by about 25 days. This is not the entire story, however, as the submm response is approximately a dust temperature response and thus the underlying protostar luminosity change should be much stronger (i.e., it is expected to be more similar to the W1 light curve; Johnstone et al. 2013; Contreras Peña et al. 2020). We therefore expect that the protostellar luminosity change during the burst event was significantly more peaked than that seen in the submm, with a half-maximum width of only days for the rise and weeks for the decay.

4. Morphology of Emission Components

In the previous section, we demonstrate that HOPS 373 is variable in the mid-IR and submm and interpret the submm variability in terms of an accretion burst. In this section, we dissect the source into distinct structures to understand the variability. In the submm, HOPS 373 has been resolved into two compact continuum sources with a small-scale CO outflow from the SW component (Figure 5). These structures together serve as benchmarks for interpreting the emission sources across wavelengths (Figure 6). In this section, we first describe the binary components and the outflow, and then describe the locations of emission in different bands.

For each instrument and image, the precise location of the emission related to HOPS 373 is determined by centroiding nearby compact sources (Table 5). The absolute images are then registered to the WISE astrometric frame. Appendix A describes the details of these positional shifts.

[19] HOPS 373 is brighter in IRAC Band 1 than W1, likely because W1 has a higher transmission than IRAC Band 1 at <3 μm. A direct comparison is challenging for HOPS 373 because of the filter mismatch.

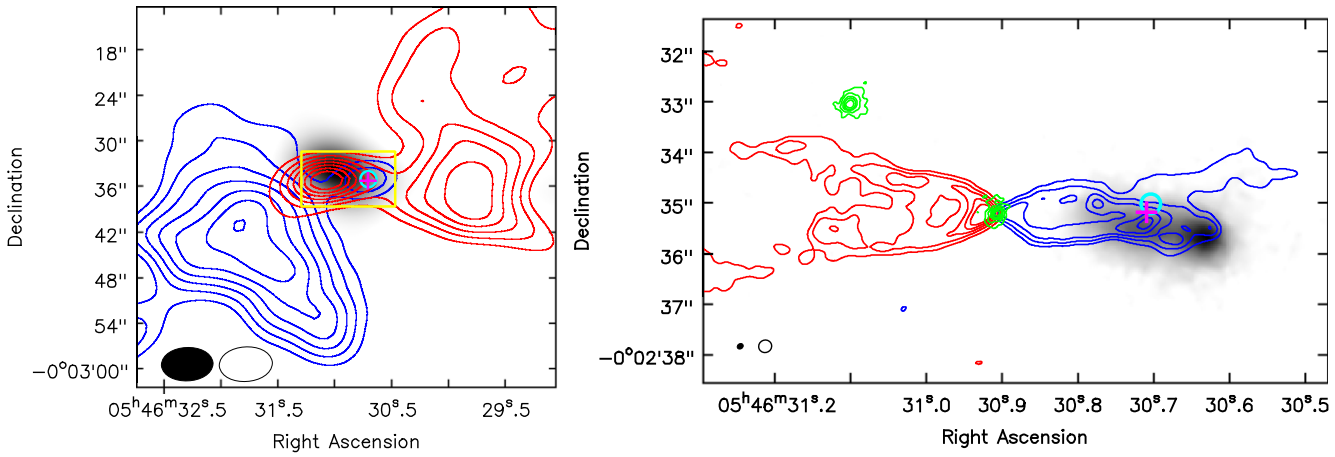

Figure 5. Left: ^{12}CO (2–1) integrated intensity map (blue contours from −6.2 to 9.0 km s^{-1}, red contours from 12.5 to 36.0 km s^{-1}) overlaid on the 1.3 mm continuum image (grayscale). The contour levels are from 4σ to 28σ in steps of 4σ, with 1σ = 2.4 Jy beam^{-1} km s^{-1}. The cross (magenta) and circle (cyan) show the median centroid of the WISE observations at the quiescent and burst phases, respectively. The yellow box is the field of view of the right panel. Right: ^{12}CO (3–2) integrated intensity and the 0.89 mm continuum maps overlaid on the Gemini North/GNIRS *K*-band acquisition image. The blue and red contours show the CO integrated emission over the velocity ranges of from −16.0 to 9.0 km s^{-1} and 13.0 to 37.0 km s^{-1}, with contour levels from 4σ to 20σ in steps of 4σ with 1σ = 0.2 Jy beam^{-1} km s^{-1}. The green contours show 0.89 mm continuum emission associated with NE and SW sources with levels of 5σ × (1, 2, 4, 6, 10, 20) with 1 $\sigma = 4.0 \times 10^{-4}$ Jy beam^{-1}. The filled and open circles in the bottom left corner present the beam size of the continuum and spectral line observations, respectively.

4.1. Binarity in the Submillimeter

High-resolution mm imaging shows two distinct continuum sources with a separation of 3.″6 and a position angle 232° (Figure 7; Tobin et al. 2015, 2020b), using the NE component as the reference point. The continuum sources seem to be surrounded by a large envelope, which is resolved out in the high-resolution image. In Figure 7, the diffuse emission surrounding the sources is associated with this unseen larger envelope.

The binary components of the 0.89 mm emission are HOPS 373 NE centered at 05:46:31.100–00:02:33.02 and HOPS 373 SW at 05:46:30.905–00:02:35.20 (Tobin et al. 2020b). The integrated fluxes of the NE and SW sources are 85.0 ± 3.3 mJy and 81.8 ± 1.7 mJy, respectively, as measured from the integrated flux in a 2D Gaussian fit of *imfit* in CASA. The total 0.89 mm emission[20] in the two continuum sources is ∼0.17 Jy, or about 9% of the integrated flux in the 850 μm emission seen in SCUBA-2. Most of the emission is resolved out with the small beam.

The ACA 1.33 mm continuum emission, obtained with a 6.″8 × 4.″4 beam, has a centroid of 05:46:30.971–00:02:34.13 between the two compact components, is elongated in the position angle of these components, and has a flux of 362 ± 9 mJy. In the Rayleigh–Jeans limit, this flux at 1.33 mm implies a flux of 886 mJy at 850 μm, or 45% of the total emission from the source. In a simulation of the ACA observation, if only the two point sources were present, they would be marginally resolved. However, the ACA continuum image shows an emission peak between the two sources, which means that some diffuse emission surrounds the two compact sources.

During the burst, the centroid of the residual (burst–quiescent) emission in the SCUBA-2 850 μm images is located 1.″1 closer to the SW component than the quiescent emission, consistent with expectations if the SW component is the source of the variability. The residual emission also has a compact profile, consistent with an FWHM[21] of ∼7″, while the quiescent emission has an FWHM of 15″ in the SCUBA-2 data.

4.2. CO Outflows

The ALMA images from the ACA and the 12 m array reveal large-scale outflows in CO 2–1 emission (see Figure 5 and also channel maps from the high-resolution 12 m array observations of the CO outflow presented in Appendix A). At large scales, the blueshifted outflow is located to the southeast of the source, while the redshifted outflow is located to the northwest (see also Mitchell et al. 2001; Nagy et al. 2020). At small scales, the outflow direction is the opposite: the blueshifted outflow is launched to the west, while the redshifted outflow is launched to the east. The small-scale outflow is driven by the southwestern component.

The position–velocity (PV) diagram (the upper panel in Figure 8) along the position angle of 90° centered on HOPS 373 SW shows that the blue- and redshifted outflows extend to 4″ from the source. CO emission is also detected in extremely high-velocity components, or bullets, in a jet-like collimated morphology with velocities of −60 and 65 km s^{-1} in each direction relative to the source velocity of 10 km s^{-1} (the lower panel in Figure 8). Such bullets are commonly detected in CO emission in jets from very young protostars (Tychoniec et al. 2019). However, because the CO (3–2) line observation was carried in 2016, the jet-like feature is not directly related to the recent outburst.

The northeastern component is not associated with any detected small-scale outflow. Any outflow from the northeastern component would have to either be low-velocity and absorbed by the cloud or large enough so that it is resolved out. The large-scale outflow is either a historical remnant of an outflow driven by the northeastern component, or the southwestern component has precessed such that the wind direction changed from red to blue. A large change in outflow direction

[20] The fluxes measured by Tobin et al. (2020b) are ∼15% higher from the same observation, due entirely to differences in subtracting the nearby emission. The compact emission in the two components is located on top of diffuse emission on scales small enough that it does not resolve out.

[21] The precise FWHM is uncertain because the profile width is much narrower than the 14.″1 beam size of SCUBA-2 at 850 μm.

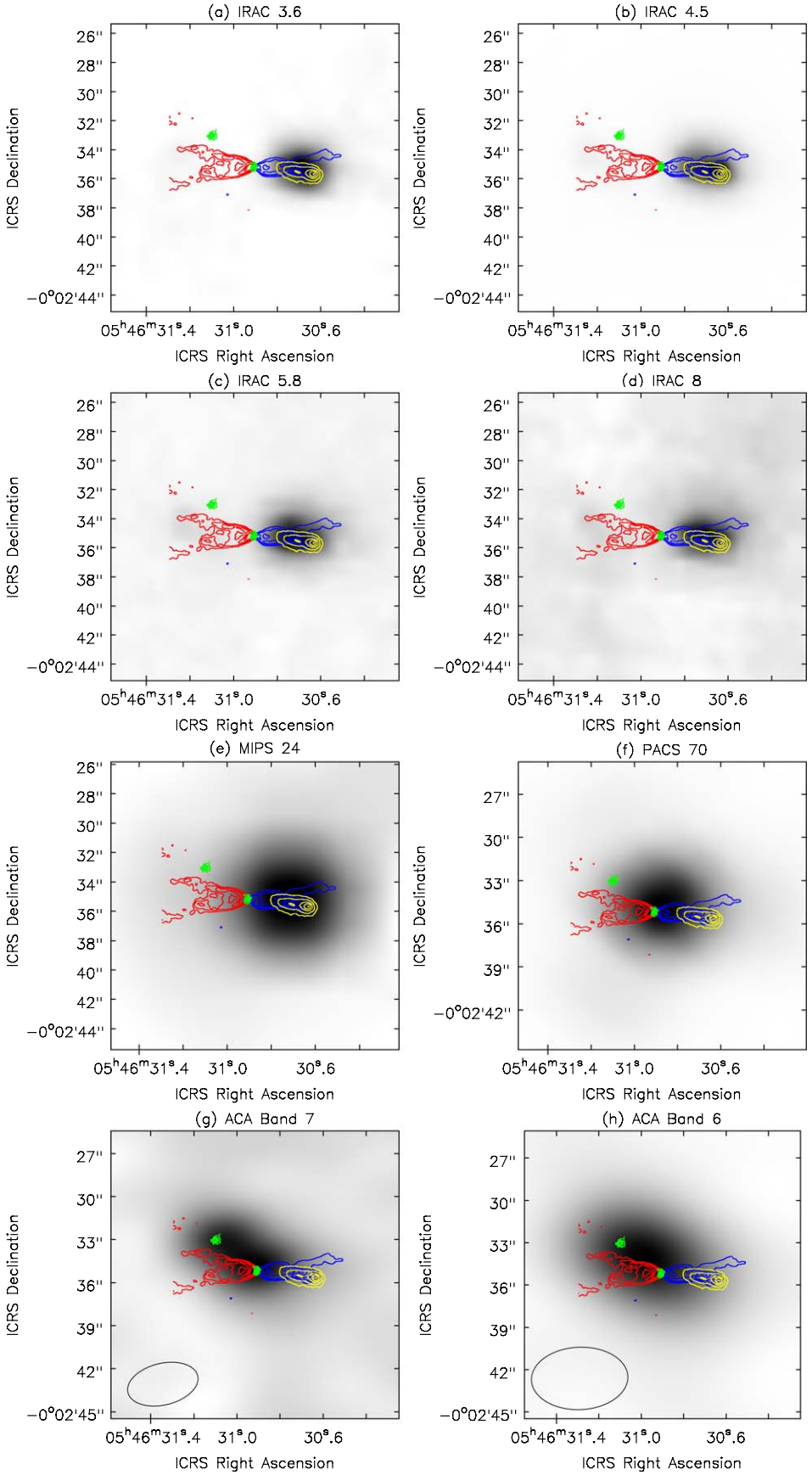

Figure 6. The ^{12}CO 3–2 (blue and red contours, following Figure 5), 0.89 mm continuum emission (green) and GNIRS Ks-band contours (yellow) map, superimposed on the (a) IRAC 3.6 μm (Band 1) image, (b) IRAC 4.5 μm (Band 2) image, (c) IRAC 5.8 μm (Band 3) image, (d) IRAC 8 μm (Band 4) image, (e) MIPS 24 μm band image, (f) PACS 70 μm band image, (g) ACA Band 7 (0.89 mm) continuum image, and (h) and ACA Band 6 (1.3 mm) continuum image.

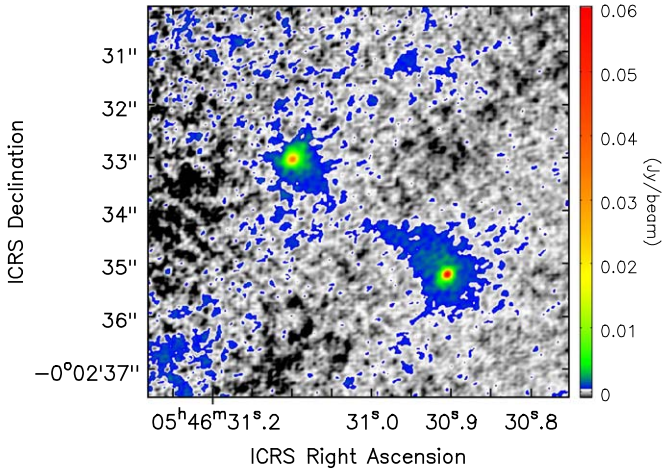

Figure 7. ALMA Band 7 (0.89 mm) continuum image of HOPS 373. The NE and SW sources show a weak extended continuum emission surrounding the compact emission.

Table 5
Centroid Positions

Instrument	λ	R.A.[a] 05 46 00+X[b]	Decl.[a] −00 02 00 −Y[b]
2MASS	1.2–2.5 μm	30.648	35.02
WISE	3–25 μm	30.705	35.23
IRAC	3.6 μm	30.686	35.26
IRAC	4.5 μm	30.692	35.26
IRAC	5.8 μm	30.709	35.16
IRAC	8.0 μm	30.698	35.07
MIPS	24 μm	30.726	35.10
PACS	70 μm	30.859	35.31
PACS	160 μm	30.855	34.87
SCUBA-2	450 μm	30.902	34.17
SCUBA-2	850 μm	30.913	34.43
ALMA ACA	1.33 mm	30.973	34.11

Notes.
[a] For the uncertainty of the centroid positions, see Appendix A.
[b] As an example, the first source is 05 46 30.648 −00 02 35.02.

has been identified in another very young protostar, IRAS 15398-3359 (Okoda et al. 2021).

4.3. Radio Emission from 0.9–5 cm

The archival observations from the VLA were obtained in 2015 October, just prior to the start of JCMT monitoring. At that time, the protostar was likely in a quiescent state, though brighter than the minimum. Our follow-up *C*-band observations in 2021 occurred about six months after the current and ongoing burst began.

Emission at 5 cm: The large VLA beam encompasses both of the distinct submm continuum sources (Figure 9). The flux density of HOPS 373 was 32 ± 6 μJy in 2015 and 47 ± 6 μJy in 2021 (see Table 6), apparently brighter during the burst, but consistent with no change to within 2σ. As detailed in Section 2.6.4, there is a systematic offset in the distribution of flux density differences and ratios measured for other sources in the field between 2015 and 2021. Therefore, we cannot be confident that the difference in flux density at *C* band represents a true variation. These uncertainties do not include the 5%–10% absolute flux density calibration uncertainty either.

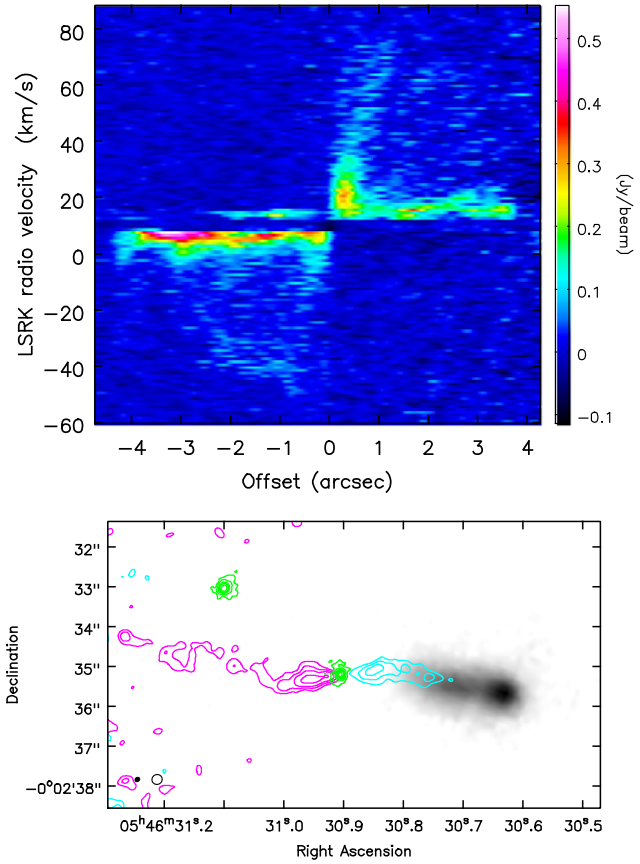

Figure 8. Top: Position—velocity diagram of CO 3–2, centered at HOPS 373 SW and aligned along the outflow axis, with a position angle of 90°. Extremely high-velocity bullets are detected within 1″ of the star in both the red- and blueshifted jets. The velocity shown here is not corrected for the source velocity of $\sim$10 km s^{-1}. Bottom: ^{12}CO (3–2) integrated intensity and the 0.89 mm continuum maps (green contours) overlaid on the GNIRS *K*-band acquisition image. Cyan and magenta contours show CO emission integrated over the velocity ranges from −50.0 to −17.0 km s^{-1} and 38.0 to 75.0 km s^{-1}, respectively, with contour levels set to (3, 5, 7, and 10) $\times$ σ, with $\sigma = 0.19$ Jy beam^{-1} km s^{-1}.

Emission at 1.3 cm: At 1.3 cm, the two continuum sources are marginally resolved when imaged at the same resolution in 2015 and 2021 (Table 6). The NE component appears brighter than the SW at 1.3 cm in 2015, while in 2021, the SW source appears to be the brighter (Figure 10), though with flux densities consistent within the uncertainties.

Emission at 0.9 cm: At 0.9 cm, the NE source is brighter than the SW source in both 2015 and 2021, but the sources are both overall brighter in 2021 relative to 2015 (Figure 10). Using the well-resolved and high S/N detections of each source at 9 mm, we find an NE/SW flux density ratio of 1.77 ± 0.13 in 2015 and 1.45 ± 0.12 in 2021, suggesting that the SW source brightened; again, a constant ratio cannot be ruled out at the 2σ level.[22] Most of the 9 mm emission is produced by thermal dust, so the brighter emission from the SW source indicates an increase in the dust temperature, in agreement with the JCMT submm observations.

[22] These ratios ignore the absolute flux calibration because this uncertainty is applied in the same way to both targets.

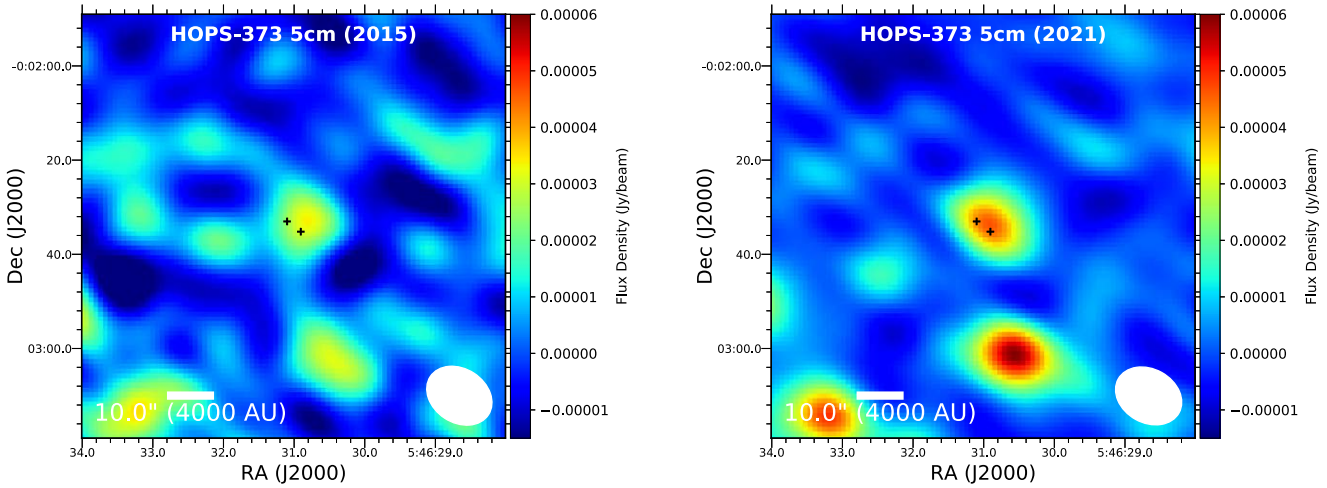

Figure 9. VLA images toward HOPS 373 at 5 cm; the 2015 data are on the left and the 2021 data are on the right. The images clearly show that the 2021 data are brighter at 5 cm, which might be a calibration issue. The positions of the SW and NE compact continuum components of HOPS 373 are marked by crosses in each panel. The beam in each image is $14\farcs77 \times 11\farcs40$.

Table 6
VLA Flux Densities[a]

λ (cm)	Flux Density 2015/2016 (μJy)	Flux Density 2021 Mar/Apr (μJy)	Flux Density 2021 May (μJy)
0.9	761 ± 24	960 ± 30	···
1.3	323 ± 10	337 ± 38	···
5.0	32 ± 6	47 ± 6	45 ± 6
NE			
0.9	486 ± 17	569 ± 21	···
1.3	170 ± 7	175 ± 27	···
SW			
0.9	275 ± 17	391 ± 21	···
1.3	153 ± 7	162 ± 27	···
H_2O Maser	(mJy km s^{-1})	(mJy km s^{-1})	
1.349	5.5 ± 0.8	56.1 ± 7	···

Note.
[a] Measured from fits with Gaussian profiles.

Emission in water masers: The water maser emission is only associated with the SW source, with a spatial position that did not change between 2015 and 2021 (Figure 10). The flux density increased by a factor of ∼10 from 2015 to 2021 (Table 6) and changed in velocity from −15 km s^{-1} in 2015 to ∼10 km s^{-1} in 2021 (relative to the local standard of rest and not corrected for the source velocity). The maser lines are narrow, with an FWHM of <1 km s^{-1} in both epochs. The previously published single-dish maser observations toward the region detected maser activity at substantially higher flux densities and at velocities of ∼20 km s^{-1} (Haschick et al. 1983).

4.4. Near- and Mid-Infrared Emission from the Outflow

The WISE W1 and W2 emission is centered $3\farcs1$ to the west of the ALMA-observed southwestern submm continuum source and is spatially unresolved due to the $\sim 6''$ point spread functions. The two epochs when HOPS 373 was bright occurred in 2019 September and 2020 September. Compared to the centroid position from previous September epochs, in 2019 the centroid position in W1 is $0\farcs176$ W and $0\farcs093$ N of previous September epochs; in 2020 the centroid is $0\farcs122$ W and $0\farcs077$ N. In W2, the offsets are $0\farcs132$ west and 0.068 north in 2019 and $0\farcs133$ W and 0.079 N in 2020. Based on previous epochs, each position has a 1σ uncertainty of $0\farcs025$. These centroid positions include the quiescent emission and the emission added from the burst. After subtracting the quiescent emission, the position of the burst would be even farther away from the quiescent centroid.

The *K*-band images of HOPS 373, mostly H_2 emission (see Section 5), are dominated by a compact source $4.2''$ west of the southwestern continuum component, with a tail of fainter emission extending back to the northeast toward the source (Figure 5). The IRAC 4.5 μm emission also shows very faint emission to the east of this source, likely associated with the redshifted outflow (Figure 2).

The *K*-band tail follows the southern half of the blueshifted CO emission. The *K*-band compact emission is located just beyond the extent of the CO emission, perhaps indicating a bow shock at the end of the jet (Varricatt et al. 2010).

The *J*- and *H*-band emission seen with UKIRT is spatially consistent with the *K*-band emission and likely traces molecular and atomic line emission from the outflow. The total source brightness is $J = 21.18 \pm 0.4$ and $H = 18.78 \pm 0.09$, but the emission is too faint to be divided into individual epochs or to be separated into different components. Spezzi et al. (2015) reported H=19.34 from the VISTA Orion Survey, fainter than measured here, either because of variability or a smaller aperture over which the emission was measured.

4.5. Far-IR Emission from the Southwest Component

The Herschel PACS 70 and 160 μm emission is nearly centered on the HOPS 373 SW (Figure 6). The binary is not resolved and the emission is not elongated in any direction. The total fluxes at 70 μm and 160 μm are 5.46 Jy and 36.3 Jy, respectively (Furlan et al. 2016). The far-IR emission seems to be mainly associated with HOPS 373 SW, attributable to the thermal emission from the HOPS 373 SW envelopes rather

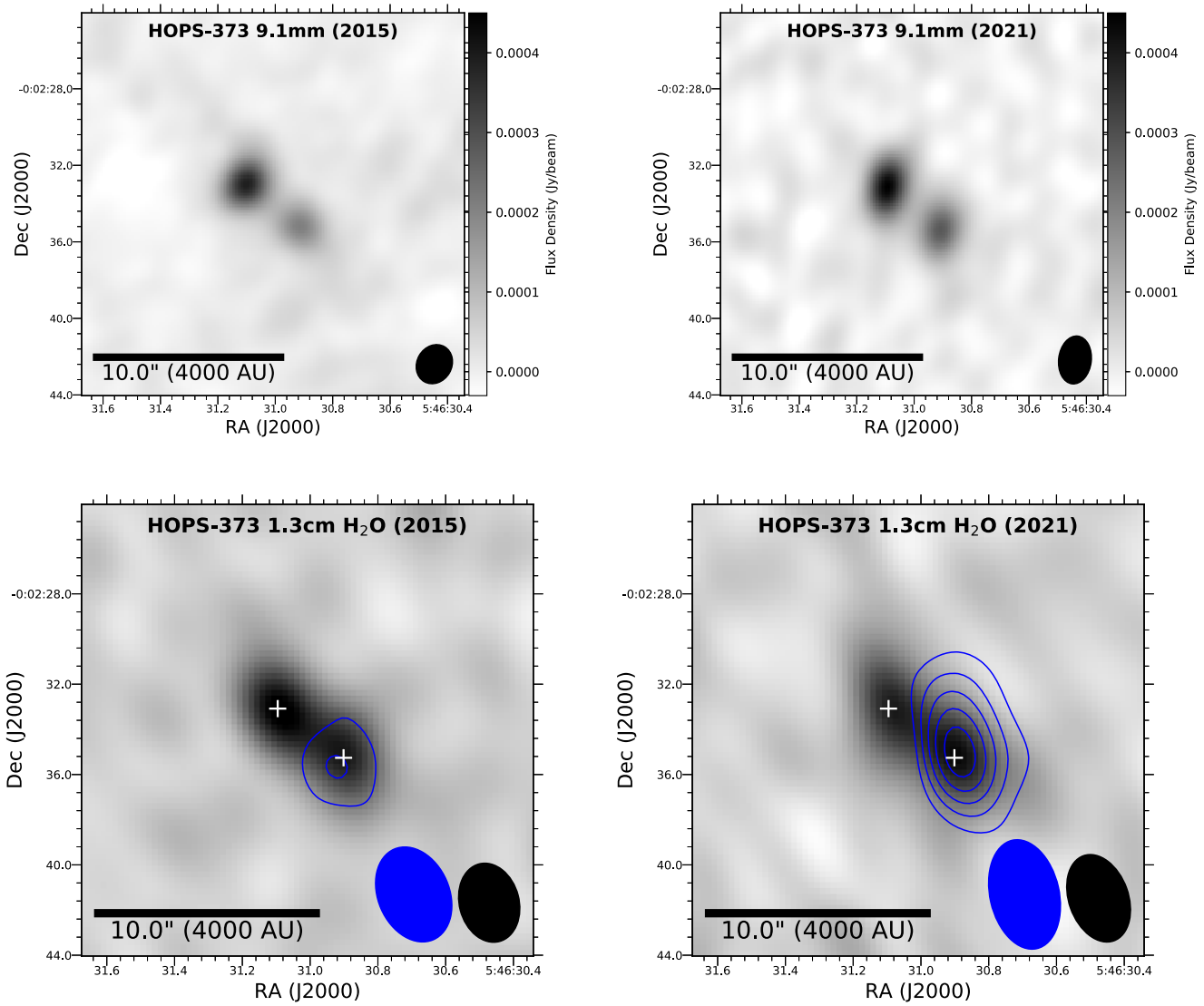

Figure 10. Top: VLA images of HOPS 373 at 9.1 mm in 2015 (left) and 2021 (right). Although both sources appear brighter in 2021, possibly because of absolute calibration error, the ratio of flux densities indicates that the SW source is brighter in 2021. Bottom: VLA images toward HOPS 373 at 1.3 cm with H_2O maser contours overlaid, in 2015 (left) and 2021 (right), both shown with the same color stretch. The positions of the NE and SW components of HOPS 373 are marked by crosses. The H_2O maser emission is associated with the SW source and brightened substantially in 2021 relative to 2015; the contours start at 3σ and increase on 2σ increments where $\sigma_{2015} = 1$ (mJy km s^{-1})/beam and $\sigma_{2021} = 4$ (mJy km s^{-1})/beam demonstrating a 7×increase in maser emission between 2015 and 2021. The 2015 maser emission is integrated from −15.5 to −14.5 km s^{-1}, and the 2021 maser emission is integrated from 9.5 to 10.5 km s^{-1}.

than to the scattered light from the cavity wall or the shocked emission seen at shorter wavelengths.

4.6. Summary of the Source Morphology

The HOPS 373 protostar consists of two compact dust sources, HOPS 373 NE and SW, separated by 3.″6, corresponding to a projected separation of 1500 au at the distance of 428 pc. The molecular outflow and maser emission are both associated with the SW component. No small-scale outflow is seen from HOPS 373 NE.

In Figure 6, we identify the location where each emission component is detected. The near- and mid-IR emission centroids are all consistent with emission located along the blueshifted outflow from the central source, where the opacity should be reduced. At 70 μm, the emission is located nearly at the position of the SW source. In the ALMA ACA Band 6 imaging at 1.33 mm, the emission centroid is located between the sources, as is the emission at ∼850 μm from SCUBA-2. The NE source does not show any emission feature over the mid-IR images. However, as the wavelength increases through the far-IR to submm, the thermal emission from each individual dust component becomes significant and the flux of the NE source increases.

The variability in the IR continuum and in the maser emission, along with the detected outflow, conclusively demonstrates that the SW component is the component that is actively accreting and variable. The variability in maser emission is consistent with past associations between maser emission and accretion (e.g., Burns et al. 2015, 2020; Hirota et al. 2021; Stecklum et al. 2021). Assuming that the maser variability is related to the accretion event, then the water masers are responding to the increase in radiation field. The masers may also brighten due to an increase in outflow activity. Any such change would occur over longer timescale than are observed for HOPS 373 and would mean that the correlation

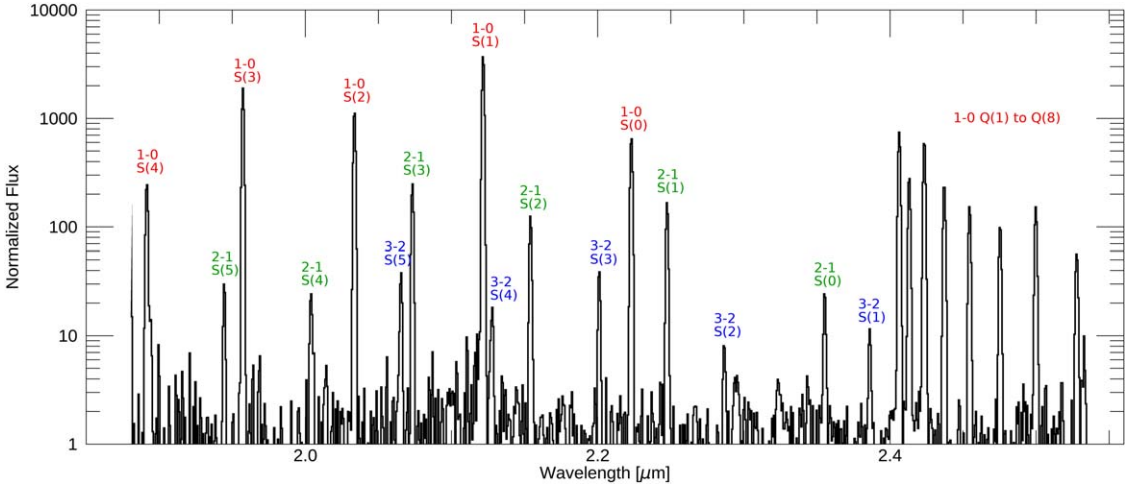

Figure 11. The normalized *K*-band spectrum of HOPS 373. The rovibrational transitions of H_2 dominate the *K*-band emission. The rovibrational transitions of $v = 1$–0, 2–1, and 3–2 are denoted with red, green, and blue labels above the lines.

between maser emission and submm emission is only a coincidence.

The NE source is only bright in the submm and is not detected in the mid-IR. The luminosity must be very low. The compact object is the size of a disk, but the central source must be low in mass and is not actively driving any outflow. The large-scale outflow may be a remnant outflow from the NE source or may be an outflow from the SW source that changed direction.

5. Molecular Emission in the Near-Infrared

The compact near-IR emission is located $\sim 4\farcs3$ away from HOPS 373 SW and is $\sim 1''$ in diameter. The elongated emission feature extends $\sim 3''$ to the east, toward the driving source. We obtained the near-IR spectrum from the compact source by placing the $0\farcs3 \times 7''$ slit nearly perpendicular to the extended near-IR emission feature (see Figure 5). The near-IR spectrum of the compact *K*-band source is dominated by rovibrational H_2 emission, detected in vibrationally excited lines up to $v = 3$ (Figure 11). Table 7 provides the intensities of the H_2 lines, measured from fitting Gaussian profiles to the lines. The flux error is estimated from the standard deviation in the continuum near each line. The H_2 1-0 S(1) line center is shifted from the central wavelength by about $-22\,\mathrm{km\,s^{-1}}$ in LSR velocity, or $\sim -32\,\mathrm{km\,s^{-1}}$ relative to the source velocity.

For an optically thin line, the intensity is proportional to the column density N_{vj} in a given rovibrational level as follows:

$$\frac{I_\lambda(v, J)}{\Omega} = \frac{Ahc}{4\pi\lambda} N(v, J) \cdot 10^{-0.4A_\lambda}, \quad (1)$$

where I is the line flux given in the unit of $\mathrm{W\,cm^{-2}}$, A is the Einstein coefficient, h is the Planck constant, c is the speed of light, N is the column density at a given rovibrational level, and Ω is the area from which the emission comes, with $0\farcs3 \times 1''$ adopted here for simplicity. The near-IR extinction to the H_2 emission is estimated to be 8.4 ± 0.1 from the H_2 line ratio of 1-0 S(1) to 1-0 Q(3) with the extinction law of $A_\lambda/A_1 = \lambda^{-2.27}$, where A_1 is the extinction at 1 μm (Maíz Apellániz et al. 2020). Other H_2 line ratios yield $A_1 = 4 - 10$ mag but are less reliable because they rely upon lines at wavelengths that are progressively longward of 2.4 μm, where our telluric correction is more uncertain. For comparison, if we adopt the extinction law of Wang & Chen (2019), with a near-IR power-law index of 2.07, the H_2 1-0 S(1) to 1-0 Q(3) line flux ratio would lead to extinctions of $A_K = 1.5$ mag and $A_1 = 7.8$ mag.

After correcting for the near-IR extinction, the H_2 $v = 1$–0, 2–1, and 3–2 rovibrational transitions are fitted with the excitation temperatures of about 2900, 1700, and 4700 K, respectively (Figure 12). A combined fit to all lines[23] leads to an excitation temperature of about 2100 K and a total column density of $4.4 \times 10^{19}\,\mathrm{cm^{-2}}$, calculated assuming a $0\farcs3 \times 1''$

Table 7
H_2 Linelist

Line ID	λ (μm)	Flux (10^{-23} W cm^{-2})	Error
1-0 S(4)	1.8919	67.3	0.9
2-1 S(5)	1.9449	4.7	0.4
1-0 S(3)	1.9576	293.8	0.4
2-1 S(4)	2.0041	3.8	0.4
1-0 S(2)	2.0338	92.0	0.1
3-2 S(5)	2.0656	2.5	0.1
2-1 S(3)	2.0735	16.5	0.1
1-0 S(1)	2.1218	168.7	0.6
3-2 S(4)	2.1280	1.8	0.3
2-1 S(2)	2.1542	8.7	0.1
3-2 S(3)	2.2014	3.7	0.2
1-0 S(0)	2.2233	77.0	0.1
2-1 S(1)	2.2477	21.8	0.3
3-2 S(2)	2.2870	1.3	0.2
2-1 S(0)	2.3556	6.0	0.3
3-2 S(1)	2.3865	3.5	0.5
1-0 Q(1)	2.4066	201.1	0.5
1-0 Q(2)	2.4134	100.2	0.5
1-0 Q(3)	2.4237	173.2	0.6
1-0 Q(4)	2.4375	96.2	0.3
1-0 Q(5)	2.4548	62.7	0.4
1-0 Q(6)	2.4756	46.1	0.9
1-0 Q(7)	2.5000	69.5	1.0
1-0 Q(8)	2.5280	30.5	2.0

[23] One outlier from the fit, $v = 1$–0 Q(5) line at 2.4548 μm, is a factor of 2.2 weaker than expected, likely because the flux overlaps exactly with a telluric absorption line. The telluric absorption line is barely seen at low resolution, but would be strong if resolved. This line is ignored in our fits.

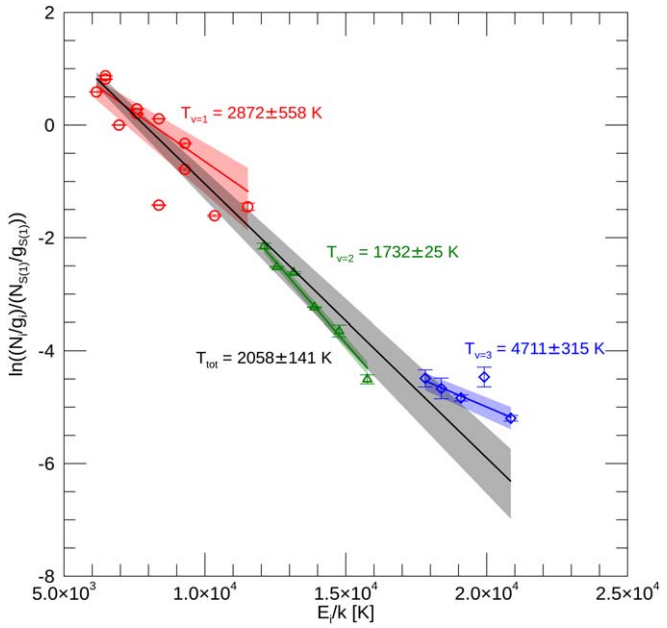

Figure 12. The excitation diagram of H_2 transitions for HOPS 373. The column densities per statistical weights of H_2 transitions are normalized by that of H_2 1-0 S(1) line. The vibrational transitions of $v = 1$–0, 2–1, and 3–2 are fitted by red, green, and blue straight lines, respectively. The H_2 1-0 Q(5) line is excluded from the fit. The total H_2 transitions are fitted by the solid black line. The shaded regions show the 3-sigma error of the fitted lines.

emitting area on the sky. These temperatures are roughly consistent with H_2 excitation temperatures from other protostellar jets (e.g., Giannini et al. 2002; Takami et al. 2006; Beck et al. 2008; Oh et al. 2018), and together with the 1–0 to 2–1 S(1) line ratio of ∼8 (Smith 1995), they indicate thermal excitation from shocks. The lines from the $v' = 3$ are somewhat stronger than thermal excitation, suggesting a possibility that populations in high vibrational levels are enhanced by UV irradiation (e.g., Black & van Dishoeck 1987; Nomura et al. 2007).

The total flux of H_2 emission in the K band between wavelengths from 2.03 to 2.37 μm is 4.0×10^{-21} W cm^{-2}, based on the best fit to all lines. This flux is 12.0 times brighter than the total continuum flux in the K band, as measured from the spectrum. Extrapolating from an H_2 excitation temperature of 2100 K and column density of 4.4×10^{19} cm^{-2}, extincted by $A_1 = 8.4$ mag, leads to H_2 fluxes of 3.21×10^{-20} W cm^{-2} in the WISE W1 band and 2.97×10^{-20} W cm^{-2} in the WISE W2 band (magnitudes of 16.8 and 15.8, respectively). Even with some correction for emission outside of the slit, these magnitudes are much fainter than the observed W1 and W2 brightness.

The CO $v = 2$-0 and 3-1 overtone bandheads are detected in emission with an integrated flux 50–90 times weaker than the summed H_2 line emission (Figure 13). These lines typically trace emission at ∼3000 K, hotter than either the submm outflow emission seen in the outflow or the warmer far-IR emission (Tobin et al. 2016). The critical density required to excite these levels, $\sim 10^{12}$–10^{13} cm^{-3} (Najita et al. 1996), is associated with dense inner disks and not with outflows.

If the W1 and W2 variability are both caused by continuum emission that scales in the same way, then ∼73% of the quiescent emission in W2 would have to be produced by lines (assuming that the lines are nonvariable). Although the H_2 component identified in the K band cannot explain such line emission at W1, a cooler H_2 emission component may be present that could contribute flux at W2, but not in W1 or in the K band (see, e.g., excitation diagrams in Giannini et al. 2006). This scenario would also be consistent with the warm (∼300 K) CO component detected in the far-IR (Tobin et al. 2016). Alternatively, strong shocks may also produce strong CO emission, as inferred in the 4–5 μm emission in photometry for the outflow shock HH 212 and the young protostar NGC 1333 IRAS 4B (Herczeg et al. 2012; Tappe et al. 2012). Strong CO fundamental ($v = 1$–0) band emission has been detected from the outflow of GSS 30 (Herczeg et al. 2011), an embedded protostar that also shows excited far-IR CO emission, like HOPS 373 (Green et al. 2013; Tobin et al. 2016).

6. The Dissection of the HOPS 373 Accretion Burst

The broadband wavelength coverage and K-band spectroscopy help us to dissect the response to an accretion burst of different structural components in the HOPS 373 protostar. In this section, we step through the different wavelengths to describe the changes in the central source, as seen at long wavelengths, and how some of that emission escapes in the outflow cavity at short wavelengths. We then describe the importance of these results for surveys that search for variable protostars.

6.1. The Submillimeter Variability and Change in Luminosity

The submm continuum emission seen with JCMT/SCUBA-2 traces dust in the envelope, heated primarily by emission from accretion onto the central protostar (see Section 3.2). Since the envelope acts as a bolometer, any change in the submm emission should probe changes in the dust temperature profile caused by variable accretion luminosity (Johnstone et al. 2013). The different scales for emission are important: the SCUBA-2 imaging has an angular resolution of 14.″1 (∼6100 au), so most of the envelope emission is detected in a single resolution element. The ALMA 12 m array observations have an angular resolution of ∼0.″08, the typical scale of protoplanetary disks, and filter out most of the envelope emission, which occurs on scales larger than ∼1″.

In the SCUBA-2 monitoring, HOPS 373 brightens by a factor of ∼1.25 at 850 μm. The single-dish SCUBA-2 and ACA submm emission is centered between the two sources. The variability is associated with the SW source, as inferred by the location of WISE mid-IR emission, ongoing outflow activity, and increase in H_2O maser emission. In the resolved ALMA observations of the continuum emission at 890 μm, obtained during a quiescent period of the NEOWISE light curve, the SW source is 88% as bright as the NE source. Nevertheless, while the NE component is bright in high-resolution submm images, the images at shorter wavelengths indicate that this source is faint and contributes little to the heating and total luminosity of the envelope. The SW component dominates the emission in the far-IR, where the combined SED peaks (Stutz et al. 2013); the SW component is also not detected at shorter wavelengths.

The bolometric luminosity of 5.3 $L_\odot$ (Kang et al. 2015), measured during a low luminosity epoch, corresponds to an accretion rate of approximately

$$\dot{M}_{\rm acc} = 1.4 \times 10^{-6} \frac{R_*}{2 \times R_\odot} \frac{0.3 M_\odot}{M_*} M_\odot \ {\rm yr}^{-1}. \quad (2)$$

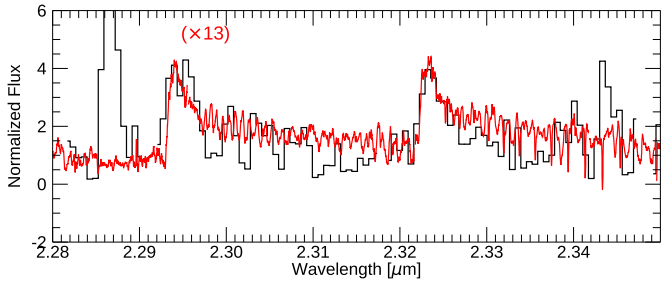

Figure 13. GNIRS CO overtone band spectrum. The IGRINS spectrum of IRAS 03445+3242 (Lee et al. 2016), multiplied by 13, is overlaid with red. The spectrum of HOPS 373 is not continuum subtracted.

The SW component is expected to contribute most of the envelope heating. With this assumption and scaling from radiative transfer models by Baek et al. (2020), the 25% brightness increase at 850 μm translates into an increase in source luminosity by a factor ~1.8. However, if both targets contribute equally to the source luminosity, and therefore to the heating of the envelope (similar to the measured ratio on small scales with ALMA), then we would infer a brightness increase of 50% at 850 μm from the southwest source. This brightening would correspond to a luminosity increase of a factor of 3.3.

Our monitoring probes only changes during what we identify as the quiescent level of emission. The far-IR CO emission is about 30 times stronger than that expected for its luminosity, based on correlations established for protostellar outflows (Manoj et al. 2016). In addition, HOPS 373 is the only PACS Bright Red Source detected in far-IR [OI] and OH emission in the Tobin et al. (2016) sample, indicating the presence of very strong shocks in the outflow.

If the high far-IR CO luminosity is associated with a photodissociation region along the outflow cavity walls, then the current internal luminosity must be,higher than that from the SED fitting, given the cooling timescales. Inspecting the SED model of HOPS 373 by Furlan et al. (2016), the model flux peaks at shorter wavelengths than the observed SED. The envelope may be more massive than ~0.3 $M_{\odot}$ (Furlan et al. 2016) because no near- and mid-IR emission is detected from the protostar itself. We estimated the envelope mass from the 850 μm flux to be ~3.6 $M_{\odot}$ by using Equation (1) in Johnstone et al. (2001) with a dust temperature of 20 K and a dust opacity of 0.01 cm^2 g^{-1} at 850 μm. The source luminosity may be underestimated if some uncertain fraction of the energy escapes the system through the outflow cavities, although any underestimate would likely be much less than the factor of 30 needed to explain the CO emission.

On the other hand, if the far-IR CO emission is dominated by the shocked gas, then the internal luminosity and far-IR CO emission might not necessarily be contemporaneous. HOPS 373 is the only one of the PRBS with strong far-IR CO and H_2O lines, along with some OH and [O I] emission (Manoj et al. 2016; Tobin et al. 2016). The ALMA observation of CO emission shows a well-collimated jet and spot-like H_2 emission along the outer boundary of CO outflows and at the termination of the outflow. These observational results indicate nondissociative C shocks, and a time difference of 1000 yrs might be possible in the consideration of shock chemistry. Other young sources, such as NGC 1333 IRAS 4B, HOPS 108, and HOPS 370, also have anomalously strong CO emission, perhaps because the emission is produced by nondissociative C-shocks (e.g., Herczeg et al. 2012; Manoj et al. 2013; Karska et al. 2018).

6.2. Interpreting the Brightness Changes in the Infrared

The warm dust and gas emission seen in the near- and mid-IR traces the outflow (see schematic from Visser et al. 2012). The H_2 emission is produced in shocks in the outflow and along the cavity walls. The continuum emission, which dominates the W1 imaging, is most likely produced by the warm inner disk, which irradiates the cavity walls, although we cannot rule out in situ emission from warm dust that could line the cavity walls. In this scenario, the mid-IR emission from the disk is detected in scattered light off the cavity walls. The high extinction through the envelope to the central star absorbs all short-wavelength emission, with a dense envelope that causes the SED to peak at 100 μm, while the line-of-sight extinction to the H_2 emission in the outflow is $A_1 = 8.4$ mag. This extinction is caused by dust in the interstellar medium and in the circumstellar envelope. The disk origin for the IR continuum emission is supported by the detection of CO overtone band emission and by the ratio of the changes in the IR compared with the submm.

The CO overtone bands ($\Delta v = 2$) in our GNIRS spectrum are likely produced in the disk (e.g., Brown et al. 2013; Ilee et al. 2013) because the critical density to excite the upper levels is higher than expected for outflow shocks. The detected CO emission would therefore be seen only because the outflow scatters emission that originates in the disk. This scenario strongly supports the idea that the W1 emission is scattered light. For the high-mass protostar IRAS 11101–5829, CO overtone emission is detected in scattered light by the outflow wall, but is generated by the disk (Fedriani et al. 2020). The high-mass protostar S255IR NIRS 3 also seems to have a similar morphology, with variability in continuum and CO emission traced to light echoes (Carattio et al. 2017). This specific scenario, with H_2 emission from extended winds and CO emission produced by the disk, but seen only in scattered light, also has a direct analog with the post-main-sequence, pre-planetary nebula IRAS 16342–3814 (Gledhill & Forde 2012).

The relation between the variability in W1 and that at 850 μm, $F_{\rm mid-IR} \propto F_{850}^{\eta}$, is $\eta \sim 4.6$ for HOPS 373, consistent with the empirical correlation found for mid-IR and submm variability for a subset of JCMT Transient Survey embedded protostars, $\eta = 5.53 \pm 0.29$ (Contreras Peña et al. 2020). This correlation is also close to expectations from radiative transfer models that include mid-IR emission from disks scattering of light off outflow cavities (Baek et al. 2020).

The variability is smaller in other IR bands, with $\eta \sim 1.8$ at W2 and $\eta \sim 0.5$ at K band (average of the bursts in Table 4). Since the K-band emission is dominated by H_2 lines, the observed variability must be produced by either large changes in the continuum emission or small changes in the H_2 emission. The continuum variability at W2 is also likely veiled by stable molecular emission, either a cool H_2 component or CO emission from a strong shock in the outflow.[24]

The raw W2 − W1 color is an extreme outlier in protostar samples (e.g., Gutermuth et al. 2009; Dunham et al. 2015). If we correct the W2 photometry by assuming that the continuum

[24] The molecular emission from shocks should be constant on relevant timescales and change only on the longer (centuries) timescales for the outflow to travel ~1000 au.

variability at W1 and W2 is the same, then the W2 continuum brightness would be 1.4 mag fainter than measured, or W2 = 12.3, during quiescence; the remaining 75% of the quiescent W2 emission is produced by either CO or H_2. The W1 − W2 color is then ∼3.1 mag, still an outlier among protostars. Compared to the variable young protostar EC 53 (W1 − W2 = 2.3 from Lee et al. 2020 and $A_V \sim 10$ from Dunham et al. 2015), HOPS 373 is 0.8 mag redder than EC 53, so if the emission sources are similar, then there should be $A_V = 60$ mag more extinction to HOPS 373 than to EC 53 (for the extinction curve of Wang & Chen 2019), so $A_V \sim 70$ mag. This excess extinction is the sum of extinction in our line of sight to the outflow emission (including any interstellar dust) and in the line between the outflow emission and the central source. While this extinction estimate is highly uncertain, the very red color even after correcting for molecular line emission indicates that either the extinction to the mid-IR emission from the outflow is high, or that the emission comes from a very cool source. The extinction of $A_V \sim 70$ mag is higher than that inferred from the H_2, but the H_2 emission in the slit is dominated by the compact source, while the mid-IR emission is centered closer to the central object. The extinction in our line of sight to the central source is probably even higher than this value.

The mid-IR (and any near-IR) continuum emission is either scattered light or produced in situ by dust along the cavity walls. If this continuum is produced by scattered light, the quiescent brightness of W1 = 15.0 would correspond to a central source brightness of W1 ∼ 6, after very roughly correcting for the scattered light, as follows. We assume that the scattering source intercepts 1% of the stellar emission (5 mag reduction in brightness) and then reradiates that emission over 4πsteradians (2.75 mag reduction). The albedo is 0.3–0.55 at 3.5 μm (Weingartner & Draine 2001), and the extinction (if it is the same as the H_2 extinction) causes a 0.3 mag reduction in brightness. The source would still have a very red W1 − W2 color, so the extinction to the mid-IR emission may be higher than that to the H_2 emission. The W2 absolute brightness would then be comparable to the bright outbursting star FU Ori (e.g., Zhu et al. 2007), in other words, very bright, but still physically plausible. Any IR emission from the central star itself is entirely attenuated by the optically thick envelope and is not directly detected. If the energy from the central source is beamed out of the cavity, the bolometric luminosity of 5–6 $L_\odot$ may be somewhat underestimated because the fluxes in the near- and mid-IR are not the total fluxes from the central protostar itself. This might be indicated by the overluminous far-IR CO emission, as discussed in Section 6.1.

An alternative to the scattering hypthesis for the IR emission is that dust emission could be produced from the cavity walls themselves. Such emission could be explained by ∼200 K dust emission throughout the observed emission area, leading to a very red spectrum with a flux that is roughly consistent with the observed brightness. In this scenario, excess luminosity from the protostar would heat the dust enough to increase the near-IR emission on light travel timescales (<10 days). However, the high density of the CO overtone emission makes it challenging to explain with in situ emission from the cavity walls. Additionally, the region where the 2000–3000 K CO emission is produced is hotter than the dust sublimation temperature, so dust emission would not be colocated exactly where the CO emission occurs. A time-dependent SED, including measurements at 5–15 μm where the albedo is much lower than at shorter wavelengths, would break the degeneracy between scattered and in situ emission.

6.3. Implications for Variability Surveys

The morphology of the emission from HOPS 373 has important implications for variability surveys that include protostars. The variability in the submm indicates a modest burst in the source luminosity by about a factor of 2 (Section 6.1), presumably due to enhanced accretion. The near- and mid-IR emission from the central protostar is too extincted to be directly detected (Section 4.4). The observed emission escapes along the outflow cavities, where the IR extinction is about 8 mag, as inferred from the H_2 lines. The change in luminosity implied by the submm variability is consistent with the level of variability seen at W1 (Section 6.2).

However, since the W1 emission emerges from the outflow cavity, any robust interpretation is empirical, depends on multiple lines of sight in a complicated geometry, and may be suspect. That the W1 emission is seen in scattered light does not necessarily affect the interpretation of the variability, unless there are optical depth changes anywhere along the lines of sight (as seen for some large outbursts, including V2492 Cyg and V346 Nor, Hillenbrand et al. 2013; Kóspál et al. 2017).

For HOPS 373, the near-IR and W2 emission are dominated by stable molecular emission, which reduces the detectability of any changes in the continuum emission. EGOs and the youngest (Class 0) protostars also have *K*-band emission that is dominated by H_2 lines (Carattio et al. 2015; Laos et al. 2021), such that any continuum variability would be veiled and not large enough to trigger follow-up. The variability in W2 is also less than expected, likely veiled by nonvariable CO and/or H_2 emission. The line emission is produced along the outflow cavity walls, detected here as H_2 and submm CO emission, and at a strong bow shock that produces H_2 emission, but no significant submm CO emission (see also far-IR CO emission; Tobin et al. 2016).

Searches for variability in the *K* band (e.g., VVV Survey; Contreras Peña et al. 2017; Lucas et al. 2017) or in W2 (Park et al. 2021) may miss variability in sources like HOPS 373. Many spectra of outbursts identified in the VVV survey show strong H_2 emission (Guo et al. 2020), although none are nearly as extreme as HOPS 373 because they would not have been identified as candidate outbursts. The variability in W1 emission should be more reliable than *K* or W2 in diagnosing changes in the warm dust emission from the disk. Any IR color analysis would indicate molecular emission rather than any spectral index for the dust continuum emission. For follow-up investigations of protostellar variables, sources that are found to have spatial offsets between the infrared and submm emission are likely to yield similar *K*-band spectra as HOPS 373, with strong H_2 emission.

6.4. Future Experiments with High-cadence Light Curves

The protostellar morphology is a confounding variable, but also a potential source of leverage because of delays caused by light travel time and opacities. If the outflow is nearly in the plane of the sky, to maximize the light travel time for IR light from the source scattered by the blueshifted outflow, then the emission at ∼3″–4″ (1400–1800 au) would by delayed by

7–9 days. Very high time resolution might be able to trace the outflow shape as the emission scatters off of dust at progressively larger distances from the central object. Such reverberation mapping has been applied to variable protostars IRAS 18148–0440 (Connelley et al. 2009), LRLL 110 (Muzerolle et al. 2013), and L1527 IRS (Cook et al. 2019). The IR light curve from the central star would only be delayed and would not be appreciably smoothed out.

On the other hand, the submm emission is expected to be delayed and smoothed out (see Section 3.2 and Johnstone et al. 2013). The energy from the central star heats the envelope, which is optically thin at 850 μm. The heating occurs in all directions away from the central star, including the far side of the envelope. Even though the envelope dust temperature equilibrates quickly, the associated light-crossing timescale for the core is about one month, and thus any short-timescale burst will be smoothed out. Competing with this relatively long smoothing function, the steep density and temperature radial gradients in the envelope make the initial submm reaction to an instantaneous burst strong, with a long, weaker tail to the response. The first burst of HOPS 373 has a submm light curve with a steep rise (<50-day doubling time), which is expected to have been broadened by the envelope heating and light propagation times—implying an underlying rise that must have been even faster. Conversely, the broader observed decay, ~75-day halving time, is not much influenced by the envelope response time. Future simultaneous, well-calibrated, and high-cadence (daily) monitoring of a protostellar burst in both the IR and submm could place much stronger constraints on the envelope structure.

7. Conclusions

In recent years, IR and submm variability surveys have been developed to search for large accretion outbursts on protostars. In this paper, we evaluated multiwavelength emission for the modest accretion burst of HOPS 373, a deeply embedded protostar in NGC 2068 in Orion, with the following results:

1. Variability in the submm continuum emission provides an indirect probe of the variability of the central source luminosity, dominated by accretion. The source luminosity brightens by ~1.8–3.3, depending on the contribution to the quiescent luminosity from the northeast source.
2. High-resolution mm imaging reveals two distinct compact sources, which complicates the conversion of submm brightness variability into changes in accretion luminosity onto the varying source. The southwest component is identified as the variable because it launches the small-scale outflow and is associated with maser emission, which is also much brighter in 2021 than in 2015.
3. The observed near- and mid-IR continuum emission is likely scattered light from the central protostar and disk scattered in the outflow cavity; similar to the spatially resolved variability in the scattered-light nebulae of low-mass stars LRL 54361 (Muzerolle et al. 2013) and L1527 IRS (Cook et al. 2019). In the IR and submm, the variable emission from the protostar and its disk cannot be detected directly.
4. For the youngest protostars, the W1 band is likely optimal for measuring continuum changes. The *K*- and W2-band emissions are dominated by CO and H_2 emission lines produced by the outflow, along the cavity walls and at a bow shock. The line emission is expected to be much more steady than the continuum emission, so these contributions will reduce any variability signal that might otherwise be measured from the continuum.

These results together indicate that photometric variability (or lack of variability) for protostars requires spectroscopic and multiwavelength investigations for physical interpretations. The *K* band and W2 band pose challenges for some subset of young protostars. Variability searches in W1 may be more reliable because of the lack of strong lines coincident with the filter transmission. With existing facilities, the submm provides the most robust measurement of protostellar variability, but is limited by sensitivity and spatial resolution and should be coupled with observations at shorter wavelengths and submm observations with high resolution.

The authors thank the referee, Phil Lucas, for a helpful and careful report. We also thank Xindi Tang, Miju Kang, Jenny Hatchell, Somnath Dutta, Ross Burns, and Jan Forbrich for helpful comments in the preparation of the manuscript.

S.Y.Y. and J.E.L. are supported by the National Research Foundation of Korea (NRF) grant funded by the Korea government (MSIT; grant number 2021R1A2C1011718). G.J.H. is supported by general grants 12173003 and 11773002 awarded by the National Science Foundation of China. D.J. is supported by NRC Canada and by an NSERC Discovery Grant. J.J.T. acknowledges support from NSF AST-1814762. M.O. acknowledges support from the Spanish MINECO/AEI AYA2017-84390-C2-1-R (cofunded by FEDER) and PID2020-114461GB-I00/AEI/10.13039/501100011033 grants, and from the State Agency for Research of the Spanish MCIU through the "Center of Excellence Severo Ochoa" award for the Instituto de Astrofísica de Andalucía (SEV-2017-0709).

The authors wish to recognize and acknowledge the very significant cultural role and reverence that the summit of Maunakea has always had within the indigenous Hawaiian community. We are most fortunate to have the opportunity to conduct observations from this mountain.

The James Clerk Maxwell Telescope is operated by the East Asian Observatory on behalf of The National Astronomical Observatory of Japan; Academia Sinica Institute of Astronomy and Astrophysics; the Korea Astronomy and Space Science Institute; the Operation, Maintenance and Upgrading Fund for Astronomical Telescopes and Facility Instruments, budgeted from the Ministry of Finance (MOF) of China and administrated by the Chinese Academy of Sciences (CAS), as well as the National Key R&D Program of China (No. 2017YFA0402700). Additional funding support is provided by the Science and Technology Facilities Council of the United Kingdom and participating universities in the United Kingdom and Canada. Additional funds for the construction of SCUBA-2 were provided by the Canada Foundation for Innovation. The James Clerk Maxwell Telescope has historically been operated by the Joint Astronomy Centre on behalf of the Science and Technology Facilities Council of the United Kingdom, the National Research Council of Canada, and the Netherlands Organisation for Scientific Research.

This paper makes use of the following ALMA data: ADS/JAO.ALMA#2015.1.00041.S and ADS/JAO.ALMA#2018.1.01565.S ALMA is a partnership of ESO (representing its member states),

NSF (USA) and NINS (Japan), together with NRC (Canada), NSC and ASIAA (Taiwan), and KASI (Republic of Korea), in cooperation with the Republic of Chile. The Joint ALMA Observatory is operated by ESO, AUI/NRAO and NAOJ. The National Radio Astronomy Observatory is a facility of the National Science Foundation operated under cooperative agreement by Associated Universities, Inc.

UKIRT is owned by the University of Hawaii (UH) and operated by the UH Institute for Astronomy. When some of the data reported here were obtained, UKIRT was supported by NASA and operated under an agreement among the University of Hawaii, the University of Arizona, and Lockheed Martin Advanced Technology Center; operations were enabled through the cooperation of the East Asian Observatory. We thank the UKIRT staff for carrying out the queue observations, and the Cambridge Astronomy Survey Unit for carrying out the WFCAM data processing.

Based on observations obtained at the international Gemini Observatory, a program of NSF's NOIRLab, which is managed by the Association of Universities for Research in Astronomy (AURA) under a cooperative agreement with the National Science Foundation on behalf of the Gemini Observatory partnership: the National Science Foundation (United States), National Research Council (Canada), Agencia Nacional de Investigación y Desarrollo (Chile), Ministerio de Ciencia, Tecnología e Innovación (Argentina), Ministério da Ciência, Tecnologia, Inovações e Comunicações (Brazil), and Korea Astronomy and Space Science Institute (Republic of Korea).

This research has made use of the NASA/IPAC Infrared Science Archive, which is funded by the National Aeronautics and Space Administration and operated by the California Institute of Technology.

Appendix A
Astrometric Shifts and Uncertainties for Accurate Positional Comparisons

The absolute astrometry for some observations may be unreliable. In each image listed in Table 8, we measure the centroid of a set of objects and then register the absolute pointing of the image based on the positions of those objects in WISE (Cutri et al. 2021).

Table 8 and 9 lists the adopted uncertainties in R.A. and decl. in each band. For 2MASS, PACS, and SCUBA-2 450 and 850 μm images, the uncertainties are measured from the astrometry using the centroids of objects presented in Table 8. The uncertainties in the WISE image are adopted from the ALLWISE catalog. Table 9 lists the uncertainties in mid-IR images ,which are estimated from the two-dimensional Gaussian fit and assuming that the astrometry is accurate.

Table 8
Centroid Positions

Object	Type[a]	R.A.(J2000)	Decl. (J2000)	ΔR.A. (″)[b]	ΔDecl. (″)[b]
		WISE Positions			
HOPS 388	Protostar	05 46 13.136	−00 06 04.85	⋯	—
LkHA 301	Disk	05 46 19.466	−00 05 20.02	⋯	—
HOPS 321	Protostar	05 46 33.184	00 00 02.03	⋯	—
HOPS 363	Protostar	05 46 43.129	00 00 52.28	⋯	—
Adopted HOPS 373		05 36 30.705	−00 02 35.23	⋯	—
		2MASS Positions			
HOPS 388	Protostar	05 46 13.135	−00 06 04.82	−0.015	0.034
LkHA 301	Disk	05 46 19.468	−00 05 19.99	0.030	0.027
HOPS 321	Protostar	05 46 33.188	00 00 02.15	0.067	0.116
HOPS 363	Protostar	05 46 43.112	00 00 52.30	−0.246	0.022
			Shift	−0.041	0.050
			Uncertainty	0.141	0.044
Adopted HOPS 373		05 46 30.648	−00 02 35.02	−0.855	0.210
		SCUBA-2 Positions[c]			
		850 μm			
LkHa 298	Disk	05 46 04.618	00 04 59.88	−0.09	1.71
V1647 Ori	FUor disk	05 46 13.140	−00 06 04.06	−0.05	0.79
LkHa 301	Disk	05 46 19.457	−00 05 18.55	−0.12	1.39
(LkHa 309)	Disk, excluded	05 47 06.861	00 00 48.81	−1.57	1.16
MGM2012 3292	Disk	05 46 18.032	00 12 12.89	0.32	0.73
		450 μm			
HOPS 315	Protostar	05 46 03.604	−00 14 47.33	−0.44	2.19
HOPS 385	Protostar	05 46 04.801	−00 14 15.20	0.24	1.49
V1647 Ori	FUor disk	05 46 13.174	−00 06 02.74	0.57	2.11
LkHa 301	Disk	05 46 19.530	−00 05 18.00	0.98	1.94
			Shift	0.18	1.54
			Uncertainty	0.42	0.52
Adopted HOPS 373	850 μm	05 46 30.913	−00 02 34.43	3.12	0.80
Adopted HOPS 373	450 μm	05 46 30.902	−00 02 34.17	2.96	1.06
		MIPS 70 μm Positions			
HOPS 388	Protostar	05 46 13.046	−00 06 04.64	−1.359	0.207
LkHA 301	Disk	05 46 19.473	−00 05 16.21	0.100	3.805
HOPS 321	Protostar	05 46 33.250	00 00 03.83	0.991	1.796
HOPS 363	Protostar	05 46 43.145	00 00 55.14	0.247	2.857
			Shift	−0.005	2.166
			Uncertainty	0.983	1.543
Adopted HOPS 373		05 46 30.916	−00 02 37.85	3.165	−2.62
		PACS 70 μm Positions			
HOPS 388	Protostar	05 46 13.128	−00 06 04.84	−0.128	0.013
LkHA 301	Disk	05 46 19.432	−00 05 19.64	−0.512	0.372
HOPS 321	Protostar	05 46 33.152	00 00 01.45	−0.485	−0.581
HOPS 363	Protostar	05 46 43.084	00 00 51.93	−0.665	−0.347
			Shift	−0.298	−0.136
			Uncertainty	0.233	0.417
Adopted HOPS 373		05 46 30.859	−00 02 35.31	2.310	−0.08
		PACS 160 μm Positions			
HOPS 388	Protostar	05 46 13.150	−00 06 05.08	0.207	−0.233
LkHA 301	Disk	05 46 19.450	−00 05 19.27	−0.243	0.751
HOPS 321	Protostar	05 46 33.291	00 00 00.62	1.609	−1.405

Table 8
(Continued)

Object	Type[a]	R.A.(J2000)	Decl. (J2000)	ΔR.A. (″)[b]	ΔDecl. (″)[b]
HOPS 363	Protostar	05 46 43.081	00 00 51.08	−0.712	−1.195
			Shift	0.215	−0.512
			Uncertainty	1.002	0.989
Adopted HOPS 373		05 46 30.855	−00 02 34.87	2.250	0.36

Notes.
[a] Classifications from Megeath et al. (2012).
[b] Offset between WISE position and measured position.
[c] SCUBA-2 450 and 850 μm images have the same pointing solution.

Table 9
Uncertainty in Centroid Positions for Mid-infrared Images

Instrument	λ	ΔR.A. (″)	ΔDecl. (″)
IRAC	3.6 μm	0.012	0.009
IRAC	4.5 μm	0.018	0.012
IRAC	5.8 μm	0.020	0.014
IRAC	8.0 μm	0.020	0.014
IRAC	8.0 μm	0.020	0.014
MIPS	24 μm	0.072	0.063

Appendix B
Channel Maps for CO Emission from HOPS 373

Figure 14 presents the channel maps for ^{12}CO 3–2 emission from HOPS 373. The blueshifted emission from the central velocity of 10.3 km s^{-1} is distributed along with the elongated feature of the GNIRS Ks emission. On the other hand, the redshifted emission shows a limb-brightened structure that traces the outflow cavity wall.

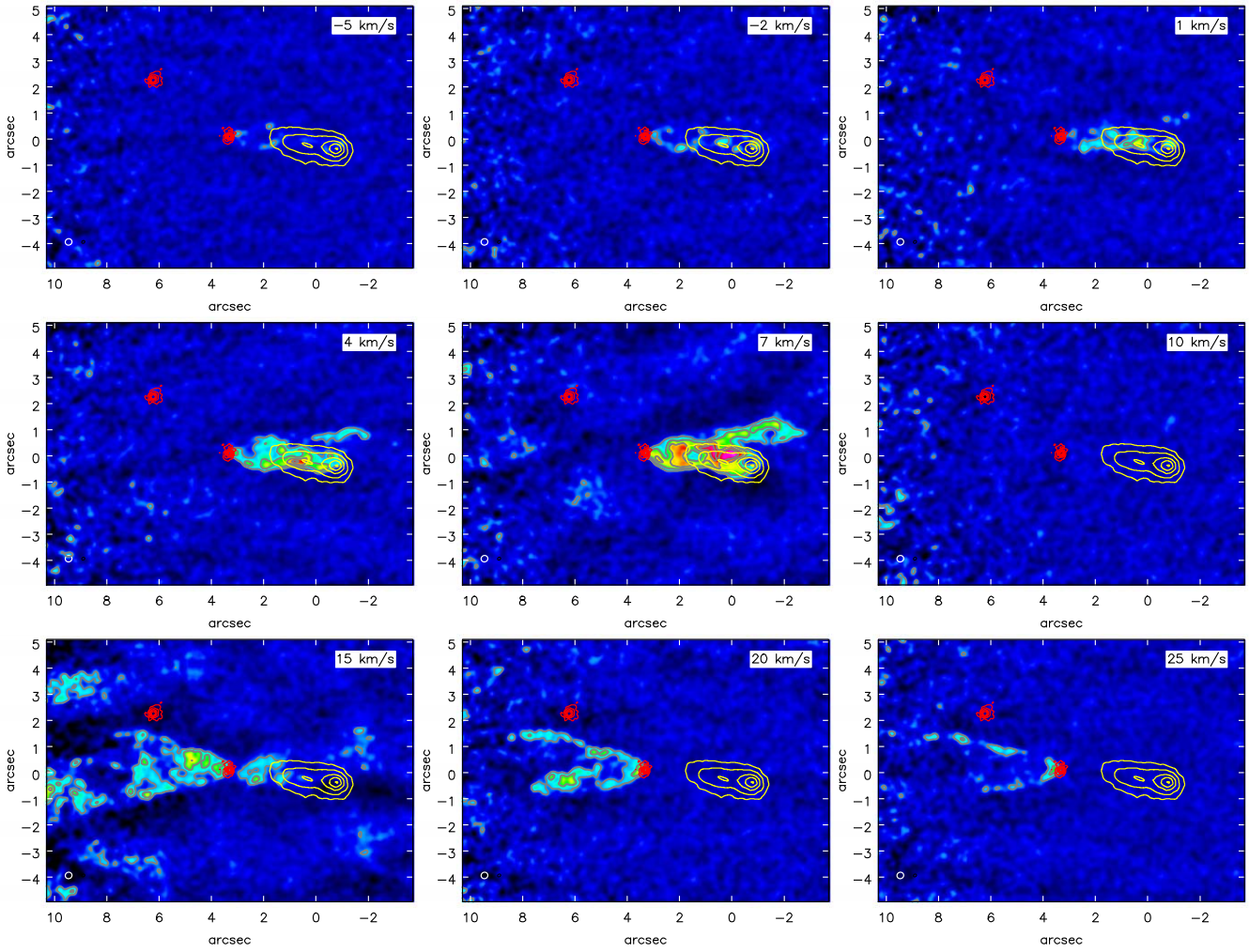

Figure 14. The ^{12}CO (3–2) channel map. The central velocity is 10.3 km s^{-1}. The gray contours show the flux density levels of $4\sigma \times$ (1, 2, 3, 4 5) with $1\sigma = 2.74 \times 10^{-2}$ Jy beam^{-1}. The 0.89 mm continuum is superposed on the map in red contours with levels of $5\sigma \times$ (1, 2, 4, 6, 10, 20) and $1\sigma = 4.0 \times 10^{-4}$ Jy beam^{-1}. The GNIRS *K*-band emission is overlaid onto the channel map with the yellow contours, in which the contour levels are 20σ, 50σ, 100σ, 150σ, and 200σ with $1\sigma = 8.4$ in arbitrary units. The beam size is presented in the bottom left corner in each panel.

ORCID iDs

Sung-Yong Yoon https://orcid.org/0000-0001-6216-0462
Gregory J. Herczeg https://orcid.org/0000-0002-7154-6065
Jeong-Eun Lee https://orcid.org/0000-0003-3119-2087
Ho-Gyu Lee https://orcid.org/0000-0002-3808-7143
Doug Johnstone https://orcid.org/0000-0002-6773-459X
Watson Varricatt https://orcid.org/0000-0002-6349-7590
John J. Tobin https://orcid.org/0000-0002-6195-0152
Carlos Contreras Peña https://orcid.org/0000-0003-1894-1880
Steve Mairs https://orcid.org/0000-0002-6956-0730
Klaus Hodapp https://orcid.org/0000-0003-0786-2140
P. Manoj https://orcid.org/0000-0002-3530-304X
Mayra Osorio https://orcid.org/0000-0002-6737-5267
S. Thomas Megeath https://orcid.org/0000-0001-7629-3573

References

Antoniucci, S., Giannini, T., Li Causi, G., & Lorenzetti, D. 2014, ApJ, 782, 51
Audard, M., Ábrahám, P., Dunham, M. M., et al. 2014, in Protostars and Planets VI, ed. H. Beuther et al. (Tucson, AZ: Univ. Arizona Press), 387
Bae, J., Hartmann, L., Zhu, Z., & Nelson, R. P. 2014, ApJ, 795, 61
Baek, G., MacFarlane, B. A., Lee, J.-E., et al. 2020, ApJ, 895, 27
Balog, Z., Muzerolle, J., Flaherty, K., et al. 2014, ApJL, 789, L38
Beck, T. L., McGregor, P. J., Takami, M., & Pyo, T.-S. 2008, ApJ, 676, 472
Black, J. H., & van Dishoeck, E. F. 1987, ApJ, 322, 412
Brown, J. M., Pontoppidan, K. M., van Dishoeck, E. F., et al. 2013, ApJ, 770, 94
Burns, R. A., Imai, H., Handa, T., et al. 2015, MNRAS, 453, 3163
Burns, R. A., Sugiyama, K., Hirota, T., et al. 2020, NatAs, 4, 506
Carattio, G. A., Stecklum, B., Garcia Lopez, R., et al. 2017, NatPh, 13, 276
Carattio, G. A., Stecklum, B., Linz, H., Garcia Lopez, R., & Sanna, A. 2015, A&A, 573, A82
Casali, M., Adamson, A., Alves de Oliveira, C., et al. 2007, A&A, 467, 777
Connelley, M. S., Hodapp, K. W., & Fuller, G. A. 2009, AJ, 137, 3494
Contreras Peña, C., Johnstone, D., Baek, G., et al. 2020, MNRAS, 495, 3614
Contreras Peña, C., Lucas, P. W., Kurtev, R., et al. 2017, MNRAS, 465, 3039
Cook, B. T., Tobin, J. J., Skrutskie, M. F., & Nelson, M. J. 2019, A&A, 626, A51
Cutri, R. M., Wright, E. L., Conrow, T., et al. 2021, yCat, 2328, 0, VizieR Online Data Catalog: II/328
Cyganowski, C. J., Whitney, B. A., Holden, E., et al. 2008, AJ, 136, 2391
Dempsey, J. T., Friberg, P., Jenness, T., et al. 2013, MNRAS, 430, 2534
Dunham, M. M., Allen, L. E., Evans, N. J., II, et al. 2015, ApJS, 220, 11
Fazio, G. G., Hora, J. L., Allen, L. E., et al. 2004, ApJS, 154, 10
Fedriani, R., Carattio Garatti, A., Koutoulaki, M., et al. 2020, A&A, 633, A128
Fischer, W. J., Megeath, S. T., Furlan, E., et al. 2020, ApJ, 905, 119
Fischer, W. J., Safron, E., & Megeath, S. T. 2019, ApJ, 872, 183
Furlan, E., Fischer, W. J., Ali, B., et al. 2016, ApJS, 224, 5
Gaia Collaboration, Brown, A. G. A., Vallenari, A., et al. 2018, A&A, 616, A1

Getman, K. V., Broos, P. S., Kuhn, M. A., et al. 2017, ApJS, 229, 28
Giannini, T., McCoey, C., Nisini, B., et al. 2006, A&A, 459, 821
Giannini, T., Nisini, B., Carattio Garatti, A., & Lorenzetti, D. 2002, ApJL, 570, L33
Gibb, A. G., & Little, L. T. 2000, MNRAS, 313, 663
Gledhill, T. M., & Forde, K. P. 2012, MNRAS, 421, 346
Green, J. D., Evans, N. J., II, Kóspál, Á, et al. 2013, ApJ, 772, 117
Guo, Z., Lucas, P. W., Contreras Peña, C., et al. 2020, MNRAS, 492, 294
Gutermuth, R. A., Megeath, S. T., Myers, P. C., et al. 2009, ApJS, 184, 18
Hartmann, L., & Kenyon, S. J. 1996, ARA&A, 34, 207
Haschick, A. D., Moran, J. M., Rodriguez, L. F., & Ho, P. T. P. 1983, ApJ, 265, 281
Herczeg, G. J., Brown, J. M., van Dishoeck, E. F., & Pontoppidan, K. M. 2011, A&A, 533, A112
Herczeg, G. J., Johnstone, D., Mairs, S., et al. 2017, ApJ, 849, 43
Herczeg, G. J., Karska, A., Bruderer, S., et al. 2012, A&A, 540, A84
Hillenbrand, L. A., Contreras Peña, C., Morrell, S., et al. 2018, ApJ, 869, 146
Hillenbrand, L. A., Miller, A. A., Covey, K. R., et al. 2013, AJ, 145, 59
Hirota, T., Cesaroni, R., Moscadelli, L., et al. 2021, A&A, 647, A23
Holland, W. S., Bintley, D., Chapin, E. L., et al. 2013, MNRAS, 430, 2513
Hsieh, T.-H., Murillo, N. M., Belloche, A., et al. 2019, ApJ, 884, 149
Tychoniec, Ł., Hull, C. L. H., Kristensen, L. E., et al. 2019, A&A, 632, A101
Ilee, J. D., Wheelwright, H. E., Oudmaijer, R. D., et al. 2013, MNRAS, 429, 2960
Johnstone, D., Fich, M., Mitchell, G. F., & Moriarty-Schieven, G. 2001, ApJ, 559, 307
Johnstone, D., Hendricks, B., Herczeg, G. J., & Bruderer, S. 2013, ApJ, 765, 133
Johnstone, D., Herczeg, G. J., Mairs, S., et al. 2018, ApJ, 854, 31
Jørgensen, J. K., Visser, R., Williams, J. P., & Bergin, E. A. 2015, A&A, 579, A23
Kang, M., Choi, M., Stutz, A. M., & Tatematsu, K. 2015, ApJ, 814, 31
Karska, A., Kaufman, M. J., Kristensen, L. E., et al. 2018, ApJS, 235, 30
Kirk, H., Di Francesco, J., Johnstone, D., et al. 2016, ApJ, 817, 167
Kóspál, Á., Ábrahám, P., Prusti, T., et al. 2007, A&A, 470, 211
Kóspál, Á., Ábrahám, P., Westhues, C., & Haas, M. 2017, A&A, 597, L10
Kóspál, Á., Szabó, Z. M., Ábrahám, P., et al. 2020, ApJ, 889, 148
Kounkel, M., Covey, K., Suárez, G., et al. 2018, AJ, 156, 84
Laos, S., Greene, T. P., Najita, J. R., & Stassun, K. G. 2021, ApJ, 921, 110
Lee, J.-E. 2007, JKAS, 40, 83
Lee, J.-E., Lee, H.-G., Shinn, J.-H., et al. 2010, ApJL, 709, L74
Lee, S., Lee, J.-E., Park, S., et al. 2016, ApJ, 826, 179
Lee, Y.-H., Johnstone, D., Lee, J.-E., et al. 2020, ApJ, 903, 5
Lee, Y.-H., Johnstone, D., Lee, J.-E., et al. 2021, ApJ, 920, 119
Lucas, P. W., Smith, L. C., Contreras Peña, C., et al. 2017, MNRAS, 472, 2990
MacFarlane, B., Stamatellos, D., Johnstone, D., et al. 2019a, MNRAS, 487, 5106
MacFarlane, B., Stamatellos, D., Johnstone, D., et al. 2019b, MNRAS, 487, 4465
Mainzer, A., Bauer, J., Cutri, R. M., et al. 2014, ApJ, 792, 30
Mainzer, A., Bauer, J., Grav, T., et al. 2011, ApJ, 731, 53
Mairs, S., Dempsey, J. T., Bell, G. S., et al. 2021, AJ, 162, 191
Mairs, S., Johnstone, D., Kirk, H., et al. 2017a, ApJ, 849, 107
Mairs, S., Lane, J., Johnstone, D., et al. 2017b, ApJ, 843, 55
Maíz Apellániz, J., Pantaleoni González, M., Barbá, R. H., García-Lario, P., & Nogueras-Lara, F. 2020, MNRAS, 496, 4951
Manoj, P., Green, J. D., Megeath, S. T., et al. 2016, ApJ, 831, 69
Manoj, P., Watson, D. M., Neufeld, D. A., et al. 2013, ApJ, 763, 83
McMahon, R. G., Banerji, M., Gonzalez, E., et al. 2013, Msngr, 154, 35
McMullin, J. P., Waters, B., Schiebel, D., Young, W., & Golap, K. 2007, in ASP Conf. Ser. 376, Astronomical Data Analysis Software and Systems XVI, ed. R. A. Shaw, F. Hill, & D. J. Bell (San Francisco, CA: ASP), 127
Megeath, S. T., Gutermuth, R., Muzerolle, J., et al. 2012, AJ, 144, 192
Mitchell, G. F., Johnstone, D., Moriarty-Schieven, G., Fich, M., & Tothill, N. F. H. 2001, ApJ, 556, 215
Motte, F., André, P., Ward-Thompson, D., & Bontemps, S. 2001, A&A, 372, L41
Muzerolle, J., Furlan, E., Flaherty, K., Balog, Z., & Gutermuth, R. 2013, Natur, 493, 378
Nagy, Z., Menechella, A., Megeath, S. T., et al. 2020, A&A, 642, A137
Najita, J., Carr, J. S., Glassgold, A. E., Shu, F. H., & Tokunaga, A. T. 1996, ApJ, 462, 919
Nomura, H., Aikawa, Y., Tsujimoto, M., Nakagawa, Y., & Millar, T. J. 2007, ApJ, 661, 334
Oh, H., Pyo, T.-S., Koo, B.-C., et al. 2018, ApJ, 858, 23
Okoda, Y., Oya, Y., Francis, L., et al. 2021, ApJ, 910, 11
Park, W., Lee, J.-E., Contreras Peña, C., et al. 2021, ApJ, 920, 132
Phillips, R. R., Gibb, A. G., & Little, L. T. 2001, MNRAS, 326, 927
Pilbratt, G. L., Riedinger, J. R., Passvogel, T., et al. 2010, A&A, 518, L1
Plunkett, A. L., Arce, H. G., Mardones, D., et al. 2015, Natur, 527, 70
Rebull, L. M., Cody, A. M., Covey, K. R., et al. 2014, AJ, 148, 92
Reipurth, B. 1989, Natur, 340, 42
Safron, E. J., Fischer, W. J., Megeath, S. T., et al. 2015, ApJL, 800, L5
Scholz, A., Froebrich, D., & Wood, K. 2013, MNRAS, 430, 2910
Smith, M. D. 1995, A&A, 296, 789
Spezzi, L., Petr-Gotzens, M. G., Alcalá, J. M., et al. 2015, A&A, 581, A140
Stecklum, B., Wolf, V., Linz, H., et al. 2021, A&A, 646, A161
Stutz, A. M., Tobin, J. J., Stanke, T., et al. 2013, ApJ, 767, 36
Szegedi-Elek, E., Ábrahám, P., Wyrzykowski, Ł., et al. 2020, ApJ, 899, 130
Takami, M., Chrysostomou, A., Ray, T. P., et al. 2006, ApJ, 641, 357
Tappe, A., Forbrich, J., Martín, S., Yuan, Y., & Lada, C. J. 2012, ApJ, 751, 9
Tobin, J. J., Sheehan, P. D., Megeath, S. T., et al. 2020b, ApJ, 890, 130
Tobin, J. J., Sheehan, P. D., Reynolds, N., et al. 2020a, ApJ, 905, 162
Tobin, J. J., Stutz, A. M., Manoj, P., et al. 2016, ApJ, 831, 36
Tobin, J. J., Stutz, A. M., Megeath, S. T., et al. 2015, ApJ, 798, 128
Varricatt, W. P., Davis, C. J., Ramsay, S., & Todd, S. P. 2010, MNRAS, 404, 661
Visser, R., Kristensen, L. E., Bruderer, S., et al. 2012, A&A, 537, A55
Wang, S., & Chen, X. 2019, ApJ, 877, 116
Weingartner, J. C., & Draine, B. T. 2001, ApJ, 548, 296
Wright, E. L., Eisenhardt, P. R. M., Mainzer, A. K., et al. 2010, AJ, 140, 1868
Zakri, W., Megeath, S. T., Fischer, W. J., et al. 2022, ApJL, 924, L23
Zhu, Z., Hartmann, L., Calvet, N., et al. 2007, ApJ, 669, 483